

Shallow depth, substantial change: fluid-metasomatism causes major compositional modifications of subducted volcanics (Mariana forearc)

1 Elmar Albers^{1*}, John W. Shervais², Christian T. Hansen¹, Yuji Ichiyama³, Patricia Fryer⁴

2 ¹*MARUM – Center for Marine Environmental Sciences, University of Bremen, Bremen, Germany*

3 ²*Department of Geology, Utah State University, Logan, UT, USA*

4 ³*Graduate School of Science, Chiba University, Chiba, Japan*

5 ⁴*School of Ocean and Earth Science and Technology, University of Hawaii at Manoa, Honolulu,*
6 *HI, USA*

7 * correspondence: Elmar Albers, e.albers@uni-bremen.de

8

9 **Abstract**

10 Mass transfer at shallow subduction levels and its ramifications for deeper processes remain
11 incompletely constrained. New insights are provided by ocean island basalt (OIB) clasts from the
12 Mariana forearc that experienced subduction to up to ~25–30 km depth and up to blueschist-
13 facies metamorphism; thereafter, the clasts were recycled to the forearc seafloor via serpentinite
14 mud volcanism. We demonstrate that the rocks were, in addition, strongly metasomatized: they
15 exhibit K₂O contents (median = 4.6 wt.%) and loss on ignition (median = 5.3 wt%, as a proxy for
16 H₂O) much higher than OIB situated on the Pacific Plate, implying that these were added during
17 subduction. This interpretation is consistent with abundant phengite in the samples. Mass balance
18 calculations further reveal variable gains in SiO₂ for all samples, and increased MgO and Na₂O at
19 one but losses of MgO and Fe₂O₃* at the other study site. Elevated Cs and Rb concentrations
20 suggest an uptake whereas low Ba and Sr contents indicate the removal of trace elements
21 throughout all clasts.

22 The metasomatism was likely induced by the OIBs' interaction with K-rich fluids in the
23 subduction channel. Our thermodynamic models imply that such fluids are released from
24 subducted sediments and altered igneous crust at 5 kbar and even below 200°C. Equilibrium

25 assemblage diagrams show that the stability field of phengite significantly increases with the
26 metasomatism and that, relative to not-metasomatized OIB, up to four times as much phengite
27 may form in the metasomatized rocks. Phengite in turn is considered as an important carrier for
28 K_2O , H_2O , and fluid-mobile elements to sub-arc depths.

29 These findings demonstrate that mass transfer from subducting lithosphere starts at low P/T
30 conditions. The liberation of solute-rich fluids can evoke far-reaching compositional and
31 mineralogical changes in rocks that interact with these fluids. Processes at shallow depths
32 (<30 km) thereby contribute to controlling *which components* as well as *in which state* (i.e.,
33 bound in which minerals) these components ultimately reach greater depths where they may or
34 may not contribute to arc magmatism. For a holistic understanding of deep geochemical cycling,
35 metasomatism and rock transformation need to be acknowledged from shallow depths on.

36

37 **1 Introduction**

38 Geologic processes in subduction zones are among the main controllers of chemical cycling (e.g.,
39 Stern, 2002, and references therein) that had and still have severe implications for the
40 geochemical evolution and differentiation of Earth. Most importantly, such processes include the
41 liberation of fluids from the subducting slab at ~70–120 km depths that then migrate into the
42 overriding plate where they provoke hydrous partial melting of the mantle. This in turn results in
43 magmatism, tholeiitic to calc-alkaline volcanism, and, over long periods of time, the formation of
44 island arcs and continental crust (e.g., Ringwood, 1969; Peacock, 1990; Taylor & McLennan,
45 1995).

46 In greater detail, it is the breakdown of hydrous minerals contained in subducting sediments and
47 hydrothermally altered igneous crust and mantle that causes the release of H_2O during prograde
48 subduction metamorphism (e.g., Poli & Schmidt, 1995). Together with the fluids, which act as
49 primary transport agents for mass in subduction systems, elements are mobilized and transported
50 into the subduction channel (i.e., the zone at the slab–wedge interface containing the subduction
51 mélange) and the mantle wedge (e.g., Bebout et al., 1999; Scambelluri & Philippot, 2001; Ulmer,
52 2001). Consequently, arc eruptives commonly exhibit a trace element signal indicative of sources
53 that include metasomatized slab-derived components (e.g., Manning, 2004; Rustioni et al., 2021).
54 Eruptives are for instance typically enriched in the incompatible elements B, K, Sr, Cs, Ba, U,
55 and Pb that are traditionally interpreted to originate from sediments and altered oceanic basement
56 and are known as the ‘slab signature’ (Perfit et al., 1980; Tatsumi & Eggins, 1995; Codillo et al.,

57 2018). Arc eruptives provide an important window into deep subduction zone processes and
58 elemental cycling, which have been in the focus of petrologic/geochemical, experimental, and
59 modeling studies over several decades.

60 Much dehydration of the subducted lithologies, however, occurs long before these reach sub-arc
61 depths. Subducting altered and hydrated basalts, for example, may contain up to 5 wt.% H₂O—
62 the bulk of which is released during the breakdown of hydrous phases as subduction
63 metamorphism causes the transformation to blueschist (~3 wt.% H₂O) and amphibolite (~1–2
64 wt.% H₂O) facies assemblages (Poli & Schmidt, 1995). H₂O release from underthrust sediments,
65 due to the compaction and release of interstitial pore waters and mineral dehydration, start as soon
66 as they are subducted (e.g., Moore & Vrolijk, 1992; Bekins et al., 1994). This liberation of fluids
67 at shallow depths is likewise accompanied by significant mass transfer. Slab-derived fluids from
68 several subduction zones have been shown to carry high loads of solutes, in particular elements
69 that are “fluid-mobile” (e.g., at the Nankai Trough or Costa Rica; see review by Kastner et al.,
70 2014).

71 Whereas slab-derived fluids could be studied at several active convergent margins, most rocks
72 that experienced (and recorded) interactions with such fluids at low- to intermediate-depth
73 subduction conditions originate from paleo-subduction settings. Based on these rocks, now
74 exposed on land, a number of studies advocate minimal fluid and element mobility at low
75 metamorphic grades (e.g., Busigny et al., 2003; Ghatak et al., 2012; see also review by G.E.
76 Bebout in Harlov & Austrheim, 2013). The only active system that provides direct insight into
77 depths of up to blueschist-facies conditions is the Mariana convergent margin. Here, recent ocean
78 research drilling efforts (Fryer et al., 2018) have recovered rocks that differ in composition from
79 what has initially been subducted. In this communication we demonstrate that these rock samples
80 are strongly metasomatized and that the changes in composition can well be explained by their
81 interaction with slab-derived fluids. Our study highlights that the metasomatism to a large degree
82 affects mineralogical assemblages of the lithologies involved, which in turn will affect deeper
83 processes such as the composition of arc magmas and geochemical cycling.

84

85 **1.1 Serpentinite mud volcanism at the Mariana forearc**

86 The Mariana Trench in the northwestern Pacific marks the subduction of the >180 My old Pacific
87 Plate beneath the Mariana forearc. Together with altered igneous crust, a ~460 m thick
88 sedimentary cover composed of siliceous ooze, volcanoclastic deposits, and pelagic clays is being

89 subducted (Plank et al., 2000; Leat & Larter, 2003). Compaction and early, low-temperature (T)
90 mineral dehydration result in the release of fluids from the incoming lithologies soon after their
91 subduction; these fluids, in turn, hydrate and serpentinize the overlying Mariana forearc mantle
92 wedge (e.g., review by Fryer, 2012). The serpentinite is partly comminuted by tectonic
93 movements and shearing processes at the slab–wedge interface, and deep faults within the forearc
94 crust and mantle facilitate the buoyancy-driven rise of the serpentinite and slab-derived fluids to
95 the forearc seafloor where these erupt in episodic mudflows. Over millions of years, the
96 mudflows have built vast mud volcanoes up to ~50 km in diameter and ~2 km high (Fryer et al.,
97 1985; Fryer et al., 1992). More than a dozen of such serpentinite mud volcanoes are distributed
98 over the forearc seafloor. They formed at varying distances to the Mariana Trench, tapping the
99 subduction channel at subduction depths of ~13–30 km and T of <80–350°C (Fig. 1; e.g., Fryer et
100 al., 1992; Oakley et al., 2008; Hulme et al., 2010). The serpentinite mud volcanism provides
101 unparalleled insight into the shallow levels of an active subduction zone.

102 Five serpentinite mud volcanoes were sampled during three scientific ocean drilling campaigns:
103 Yinazao (55 km distance to the Mariana Trench, ~13 km depth to the slab, ~80°C at the slab–
104 mantle wedge interface), Fantangisña (62 km to trench, ~14 km to slab, ~150°C), and Asùt
105 Tesoru (72 km to trench, ~18 km to slab, ~250°C) during International Ocean Discovery Program
106 (IODP) Expedition 366 (Fryer et al., 2018), and South Chamorro and Conical (78 and 86 km to
107 trench, 18 and 19 km to slab, respectively, with $T = 250–350^\circ\text{C}$ at the slab) during previous
108 Ocean Drilling Program (ODP) legs (e.g., Fryer et al., 1992).

109 Beside serpentinite mud, recovered drill cores contain up to meter-sized boulders of the
110 serpentinized mantle wedge but also materials that originate from the forearc crust and from the
111 subducting Pacific Plate (see next section).

112 Similar mud flow deposits have been described worldwide from subaerially exposed forearc
113 regions as old as 3.8 By (e.g., Lockwood, 1972; Fryer et al., 1995; Giaramita et al., 1998; Pons et
114 al., 2011; Wakabayashi, 2012), implying that serpentinite mud volcanism in forearc environments
115 occurred throughout the geologic past but requires specific, considerably deformed non-
116 accretionary convergent margin settings.

117

118 **1.1.1 Serpentinite mud volcanism recycles subducted volcanics**

119 Rock fragments and clasts with mid-ocean ridge basalt (MORB) and ocean island basalt (OIB)
120 provenances were discovered in cores from the serpentinite mudflows of several mud volcanoes.

121 The materials vary in size from millimeter to meter scale and have been identified as subducted,
122 metamorphosed, and recycled materials from the incoming Pacific Plate. Metamorphic mineral
123 assemblages attest up to blueschist facies peak metamorphic conditions (e.g., Maekawa et al.,
124 1993; Fryer et al., 2006; Ichiyama et al., 2021). Numerous such metamafic rocks were recently
125 retrieved from the Yinazao, Fantangisña, and Asùt Tesoru mud volcanoes (Fryer et al., 2018). In
126 addition, similar clasts have previously been sampled from South Chamorro and Conical
127 Seamounts (e.g., Fryer et al., 1992). These materials are, to our knowledge, the only blueschist-
128 facies rocks that have been recovered from any active subduction zone.

129 Petrographic descriptions and (mineral) geochemical compositions of the recycled OIBs from
130 Fantangisña and Asùt Tesoru have been reported by Albers et al. (2019), Fryer et al. (2018,
131 2020), Deng et al. (2021), and Ichiyama et al. (2021). In many samples, aphyric to coarse grained
132 igneous textures are preserved; aside from rare relict Ti-rich augite, plagioclase, and traces of
133 olivine, apatite, biotite, and Fe–Ti oxides, the igneous mineral assemblages are largely
134 metamorphosed. The clasts are now composed of low- to high-*P* and low- to moderate-*T*
135 metamorphic minerals. These include Ca pyroxene, Na and Ca–Na amphibole, pumpellyite, and
136 phengite at both seamounts, with prehnite, calcite, and zeolites (analcime, thomsonite, natrolite)
137 exclusively reported from Fantangisña and lawsonite and Na pyroxene from Asùt Tesoru (Albers
138 et al., 2019; Fryer et al., 2020; Ichiyama et al., 2021). Metamorphic vein precipitates that formed
139 in apparent equilibrium with slab-derived fluids include pectolite and prehnite at Fantangisña and
140 lawsonite and phengite at Asùt Tesoru; metamorphic calcite and aragonite occur at both settings
141 (Albers et al., 2019). Na pyroxene mainly ranges in composition from aegirine to jadeite, but
142 some analyses exhibit an increased augite component; amphibole is riebeckitic with ferric Fe/Al
143 ratios of up to ~0.45 indicating a strong glaucophane component; phengite is Si-rich with up to
144 3.88 Si per formula unit (Albers et al., 2019; Fryer et al., 2020; Deng et al., 2021; Ichiyama et al.,
145 2021). These phase assemblages and compositions led Ichiyama et al. (2021) to suggest peak
146 metamorphic grades of prehnite–pumpellyite facies for the clasts from Fantangisña Seamount and
147 of blueschist facies for those from Asùt Tesoru.

148 The OIB origin of the clasts is implied by bulk rock Ti/V ratios between 50 and 100 (Fig. 2; Fryer
149 et al., 2020; Deng et al., 2021; note that the Ti–V discrimination diagram was recently revised by
150 Shervais, 2021) and by the presence of titanium augite (e.g., Albers et al., 2019). Geochemically,
151 concentrations of SiO₂, MgO, and Na₂O in the recycled OIBs appear to generally overlap with
152 those of volcanic seamounts situated on the Pacific Plate but Fe₂O₃* (= FeO + Fe₂O₃) and CaO
153 are generally lower whereas K₂O and loss on ignition (LOI) are much higher (Fig. 3 & Tab. 1;
154 Fryer et al., 2018; Deng et al., 2021). These distinct compositions have, however, not been in the

155 focus of the above studies. In this work, we will focus on the (modified) compositions of the
156 recycled OIBs, which we attribute to fluid metasomatism that occurred in the subduction zone,
157 and its implications for mass transfer and geochemical cycling.

158

159 **2 Methods**

160 **2.1 Bulk rock geochemistry**

161 To expand the existing dataset by Fryer et al. (2018) and Deng et al. (2021) we have analyzed
162 four additional OIB samples for their major element bulk compositions. Analyses were carried
163 out with a Panalytical® 2400 sequential X-ray fluorescence spectrometer at Utah State University
164 using methods described in Shervais et al. (2019).

165

166 **2.2 OIB reference compositions**

167 As reference OIB compositions we downloaded data from the PetDB Database
168 (www.earthchem.org/petdb) on 16-02-2021. We extracted all entries with the label ‘Seamount’
169 situated in the Pacific Ocean ($n = 3,216$). We then narrowed down the composition representative
170 for alkali basalt/OIB by filtering (i) for Ti/V ratios between 50 and 100 ($n = 75$) following the
171 discrimination method developed by Shervais (1982; note that Shervais, 2021, recently revised
172 the field indicating plume-derived basalts to Ti/V = 43–100); (ii) for MgO within 8–16 wt% ($n =$
173 437) to minimize crystal fractionation and accumulation effects (cf., e.g., Jackson & Dasgupta,
174 2008); (iii) a combination of the two, i.e., Pacific seamount compositions run through a Ti/V–
175 MgO-filter ($n = 17$); (iv) filtering for seamounts in the northern hemisphere only ($n = 1703$). In
176 addition, we compiled compositions of seamounts located in the northwestern Pacific Ocean, east
177 of the Izu–Bonin–Mariana subduction zone. These include data from the Magellan Seamounts
178 (Koppers et al., 1998; Tang et al., 2019; Liu et al., 2020), the Marshall Seamounts (Davis et al.,
179 1989), and from drill core recovery from Deep Sea Drilling Project Site 61, west of the Magellan
180 Seamounts (Janney & Castillo, 1999), and ODP Sites 865 and 866, the Allison Guyot and
181 Resolution Guyot at the Mid-Pacific Mountains (Baker et al., 1995). This latter compilation has
182 91 entries, of which we excluded the upper and lower 5% to account for outliers. Generally, most
183 of these rocks have undergone various degrees of hydrothermal alteration; in particular the
184 seamounts from the NW Pacific, which are up to Cretaceous in age, likely interacted with

185 seawater over millions of years. Median compositions of the reference OIBs are presented in
186 Tab. 2.

187

188 **2.3 Theriak/Domino thermodynamic modeling**

189 Equilibrium assemblage diagrams, commonly termed pseudosections, and mineral abundances
190 were calculated using the Theriak/Domino software package, Version 15-03-2018 (de Capitani &
191 Brown, 1987; de Capitani & Petrakakis, 2010). Calculations are based on the internally consistent
192 thermodynamic database tcds62 from Holland & Powell (2011), but we suppressed the formation
193 of microcline, julgoldite (FeFe), and iron as they were not observed in the recycled OIBs. The
194 database comes with solid solutions for olivine, ortho- and clinopyroxene, spinel, feldspar, biotite,
195 epidote, phengite, chlorite, and chloritoid (Baldwin et al., 2005; Holland & Powell, 1998; Holland
196 & Powell, 2003; White et al., 2007; White et al., 2014a; White et al., 2014b). It does not contain
197 thermodynamic data for K-containing amphibole, which should theoretically result in an
198 overemphasis of K-bearing white mica; however, K₂O contents in amphibole in the metamafics
199 recovered from the serpentinite mud volcanoes are negligible (e.g., Tab. 1 in Fryer et al., 2006; SI
200 in Ichiyama et al., 2021) so that we assume that, if at all, the overemphasis of mica is minor.

201 Our computations account for the oxide components SiO₂, Al₂O₃, FeO, MgO, CaO, Na₂O, K₂O,
202 and H₂O. Equilibrium assemblage diagrams were compiled for $P = 1\text{--}10$ kbar, corresponding to
203 up to ~35 km depths when assuming an average lithospheric density of 3×10^3 kg/m³, and
204 $T = 100\text{--}600^\circ\text{C}$. Such P/T range covers the conditions of the slab beneath the Mariana
205 serpentinite mud volcanoes but also the conditions in “warm” subduction zones (Peacock &
206 Wang, 1999). Mineral abundances were calculated for a geotherm of $8^\circ\text{C}/\text{km}$ as the equilibrium
207 assemblage of this geotherm best overlaps with the observed mineralogy in the recycled OIBs.
208 Diagrams were compiled for (i) the median composition of NW Pacific seamounts (Tab. 2),
209 which was recalculated to Si 49.51, Al 20.09, Fe 4.67, Mg 10.27, Ca 10.44, Na 5.90, K 1.57, and
210 H 22.65 to use as input for Theriak/Domino, and (ii) the median composition of the recycled OIB
211 clasts (Tab. 1), recalculated to Si 47.60, Al 16.92, Fe 3.47, Mg 9.65, Ca 8.03, Na 4.77, K 5.79,
212 and H 35.02. Additional O was added in both cases to account for the presence of Fe₂O₃ in the
213 hydrothermally altered rocks.

214

215 **3 Results**

216 3.1 Mass balance constraints on compositional changes

217 The major elemental compositions of the recycled OIBs reveal K_2O contents (mostly between
218 3.7–5.5 wt%) and LOI (4.0–7.7 wt%) as a proxy for H_2O that are much higher than in OIB from
219 the Pacific Ocean (Fig. 3; see also Fig. S1 for anhydrous compositions). By contrast, Fe_2O_3 and
220 CaO in the recycled OIBs appear generally lower. Patterns in Al_2O_3 , MgO , and Na_2O are
221 inconsistent: clasts from Fantangisña appear to have less Al_2O_3 , more MgO , and similar Na_2O
222 relative to Pacific OIB whereas clasts from Asùt Tesoru have similar or higher Al_2O_3 contents but
223 less MgO and Na_2O .

224 To assess the approximate changes in major element contents of the recycled OIBs, we compared
225 them with basaltic seamounts from the northwestern Pacific (Tab. 2), i.e., variably altered
226 seamounts prior to subduction at the Izu–Bonin–Mariana subduction system (referred to as
227 ‘unsubducted OIB’ from here on). It can be expected that the recycled OIBs were compositionally
228 similar to these unsubducted OIB prior to subduction. Results of our isocon analysis (Gresens,
229 1967; Grant, 1986) are shown in Figure 4; calculations were done on an anhydrous basis. The
230 results imply the addition of K_2O and variable amounts of SiO_2 to clasts from both seamounts and
231 of MgO to OIBs from Fantangisña when constant mass is assumed. The assumption of constant
232 mass appears reasonable for Asùt Tesoru where TiO_2 and Al_2O_3 , both considered rather immobile
233 at shallow subduction levels (e.g., Manning, 2004), lie on the isocon line. At Fantangisña,
234 however, this assumption would suggest the loss of all immobile species—which is unlikely. We
235 hence calculated additional isocon lines assuming the conservation of Al_2O_3 (Fig. 4; Tab. 3). The
236 median slope of these isocon lines at Asùt Tesoru ($y = 1.006x$) is almost identical to the one
237 assuming constant mass ($y = x$). It is, however, much less steep at Fantangisña ($y = 0.747x$);
238 but we argue that this assumption is reasonable here since the immobile TiO_2 plots well on this
239 line of Al_2O_3 conservation. It hence appears (i) that a net increase in mass affected the clasts from
240 Fantangisña but not from Asùt Tesoru and (ii) that the recycled OIBs from Fantangisña gained
241 K_2O , SiO_2 , MgO , and Na_2O whereas those from Asùt Tesoru gained K_2O and some SiO_2 but lost
242 Fe_2O_3 and possibly MgO . The bulk of these changes can likely be ascribed to metasomatic
243 processes that accompanied fluid–rock interactions within the subduction system (see discussion).

244

245 3.2 Equilibrium assemblage diagrams

246 Equilibrium assemblage diagrams compiled for the median compositions of unsubducted OIB and
247 the recycled OIBs illustrate which phases are to be expected in these rocks. The section for the

248 unsubsucted OIB thereby serves as a reference to determine the mineralogical consequences
249 induced by the compositional changes that we ascribe to fluid-metasomatism.

250 For the unsubsucted OIB, quartz, feldspar, pyroxene, epidote, and chlorite are predicted to be
251 stable throughout most of the modeled P/T conditions (Fig. 5a). Prehnite may form below
252 ~ 3 kbar/200°C. At higher T , biotite and tremolitic amphibole become part of the mineral
253 assemblage. Pumpellyite exists at low T and up to ~ 10 kbar, together with riebeckitic amphibole
254 and lawsonite at $P > \sim 3$ kbar. Glaucofane amphibole joins the assemblage at ~ 4.5 kbar/100°C,
255 persisting between ~ 200 – 300 °C to higher P . Phengite is restricted to $T < 350$ °C. The equilibrium
256 assemblage predicted for the recycled OIBs strongly differs from this (Fig. 5b). Quartz is absent
257 except for low- P /high- T conditions, tremolite is not predicted at all, and epidote will not form at T
258 < 200 °C. Biotite is present throughout the model conditions, except for intermediate P and $T <$
259 ~ 200 °C. Prehnite exists up to ~ 4 kbar/350°C, vesuvianite may form at T up to 450°C, and the
260 stability field of pumpellyite is restricted. Riebeckite and glaucofane form at > 2 kbar/low T , and
261 lawsonite at high P /low T . Phengite is stable throughout most of the modeled P/T range.

262 In unsubsucted OIB, the equilibrium assemblage along the 8°C/km geotherm is dominated by
263 feldspar, quartz, and epidote until ~ 6 kbar/150°C, accompanied by minor chlorite and pumpellyite
264 (Fig. 6a). Lawsonite and amphibole contents increase at $T > 150$ °C and at 170–200°C the amount
265 of pumpellyite decreases whereas that of pyroxene increases. Amphibole is tremolitic to
266 riebeckitic below ~ 6 kbar/150°C, and mainly glaucofane at higher P/T conditions (Fig. S3a).
267 Above ~ 7 kbar/200°C, the mineral assemblage consists of epidote, amphibole, quartz, lawsonite,
268 and pyroxene (mainly diopside in composition; Fig. S3a). About 1.5 mol of phengite exists
269 throughout the prograde path. Contrastingly, with 5–6 mol phengite and > 3 –4 mol pyroxene
270 present along the 8°C/km geotherm, these two phases dominate the mineral assemblage in the
271 recycled OIBs (Fig. 6b); above 200°C, pyroxene contents even increase to ~ 9 mol. Diopside and
272 aegirine components in pyroxene are predicted below 200°C, and jadeite pyroxene joins this
273 assemblage at higher P/T conditions (Fig. S3b). Lawsonite is stable even at 3.5 kbar/100°C but is
274 most abundant at $T > 200$ °C. Minor amounts of riebeckitic amphibole are formed at $T < 200$ °C
275 and moderate to minor amounts of glaucofane at $T > 150$ °C (Fig. S3b). Chlorite and feldspar
276 exist up until 6 kbar/160°C, and the presence of pumpellyite is restricted to ~ 160 °C at 6 kbar and
277 220°C at 8 kbar. Up to ~ 7 kbar/200°C, minor amounts of vesuvianite are predicted; in case
278 vesuvianite is not allowed to form in the models, pyroxene and pumpellyite contents increase at T
279 < 200 °C whereas the lawsonite content decreases (see Fig. S4 and discussion in the figure
280 caption).

281

282 4 Discussion

283 4.1 Transfer of mass within the Mariana forearc

284 4.1.1 Subduction metasomatism vs. seafloor alteration processes

285 It has long been known that subduction zones are sites of major mass transfer and chemical
286 cycling. The meta-OIB data reported by Fryer et al. (2018), Deng et al. (2021), and in this study
287 provide direct evidence for mass transfer at shallow levels of the Mariana convergent margin.
288 Most striking are increases in K₂O and LOI, but our mass balance calculations imply that SiO₂,
289 MgO, and Na₂O are also modified (Fig. 4; Tab. 3).

290 In general, subducting lithologies undergo prograde metamorphic phase changes in response to
291 rising *P* and *T* with increasing depth. Such transformations could (theoretically) occur in
292 geochemically closed systems, in which the phase assemblages of the subducting lithologies
293 would change, but the bulk rock would retain its composition. Contrastingly, fluid-induced
294 metasomatism can lead to the transfer of mass into or away from individual pieces of rock,
295 modifying their bulk composition. Absolute increases in certain elements should hence be mainly
296 the result of the interaction with fluids that transported the respective elements; losses in element
297 concentrations are usually ascribed to the breakdown of out-of-their-stability-field minerals and
298 the fluid-mediated removal of the released elements (e.g., Putnis & Austrheim, 2010).

299 Quantitatively assessing the compositional changes of the recycled OIBs remains difficult
300 because their exact compositions prior to subduction are unknown. It can be assumed that they
301 were generally similar to OIB situated in the northwestern Pacific Ocean—but the compositions
302 of such vary to a certain degree as analyzed sample suites usually cover a range of primary and
303 secondary processes (such as magmatic differentiation and crystal accumulation effects or
304 hydrothermal alteration, respectively; cf. Fig. 3; see also Figs. S2). The problem of attributing
305 compositional changes to fluid–rock interactions within the subduction zone becomes particularly
306 clear when considering, for instance, MgO contents in the recycled OIBs of which most overlap
307 with that of the unsubducted OIB (Figs. 3 & S1). The relatively higher values at Fantangisña
308 (median = 10.3 wt% vs. 4.5 wt% at Asùt Tesoru) could potentially be explained by the
309 aforementioned primary or secondary processes. Indeed, when compared to the MgO–Ti/V-
310 filtered data of all Pacific seamounts, some samples contain up to ~12 wt% MgO (gray diamonds
311 in Fig. 3). By contrast, K₂O contents of the recycled OIBs (median = 4.5 wt% at Fantangisña and
312 4.7 wt% at Asùt Tesoru) clearly exceed those of unsubducted seamounts (up to 4 wt%; median =

313 1.15 wt%), so that it appears very unlikely that these enrichments have been induced prior to
314 subduction. Similarly, we argue that SiO₂ (median = 48.2 wt% in the recycled OIBs; median =
315 50.9 wt% on an anhydrous basis) has been added to most clasts during subduction: hydrothermal
316 alteration of basalts at the seafloor admittedly also increases SiO₂ (e.g., Staudigel et al., 1996) and
317 similar contents in unsubducted OIB are not uncommon (50% of data between 44.6–47.2 wt.%;
318 Figs. 3 & S1), but the observed gains in K₂O and H₂O would dilute these values to <<46 wt%.
319 Our isocon analysis further imply that Na₂O was gained in the OIBs from Fantangisña whereas
320 Fe₂O₃* was lost from those from Asùt Tesoru (Fig. 4).

321 Altogether, it cannot be excluded that some of the differences between unsubducted and recycled
322 OIBs represent a sampling bias and/or seafloor alteration processes. But in particular the increases
323 in K₂O and H₂O, as well as, to a lesser extent, SiO₂ and Na₂O can presumably be attributed to
324 fluid-metasomatism during subduction. This transfer of mass can be well explained by the
325 presence of solute-laden fluids in the Mariana forearc that are particularly abundant and well
326 documented (e.g., Mottl et al., 2004; Savov et al., 2007; see below). The lateral distance of >160
327 km between the Fantangisña and Asùt Tesoru Seamounts, together with the fact that K₂O–SiO₂-
328 enriched OIBs were recycled at both sites, suggests that the metasomatic processes are not a local
329 phenomenon but are widespread in the Mariana Subduction System.

330

331 **4.1.2 Shallow subduction fluid processes and OIB alteration**

332 Fluid and solute release following mineral breakdown reactions in the subducting slab can be
333 traced at the outer Mariana forearc by slab-derived fluids that expel at the serpentinite mud
334 volcano summits. The compositions of these slab-derived fluids systematically change across the
335 forearc, in response to prograde metamorphic processes at depths of ~10–30 km and $T = <80$ –
336 350°C (e.g., Mottl et al., 2004; Savov et al., 2007; Hulme et al., 2010; Fryer et al., 2018). The
337 inferred processes in the slab range from sediment compaction and opal-CT dehydration at
338 shallowest levels to clay diagenesis and dehydration, the release of desorbed water, and
339 decarbonation at greater depths (Mottl et al., 2004; Hulme et al., 2010; Menzies et al., 2021). The
340 decarbonation of subducted sediments and AOC (altered igneous portions of the oceanic crust),
341 for example, is thought to result in high carbonate alkalinity in slab-derived fluids of the deeper-
342 sourced mud volcanoes relative to shallow-sourced ones. High alkalinity in turn favors the
343 precipitation of CaCO₃ below the deep-sourced mud volcanoes, leading to a depletion of Ca and
344 Sr in the fluids that rise to the forearc seafloor. By contrast, Ca and Sr in pore waters at the
345 shallower-sourced mud volcanoes are enriched because the slab is still too cold for decarbonation

346 to occur (Mottl et al., 2004). Expressed in numbers, Ca decreases from >50 mmol/kg to <1
347 mmol/kg and Sr from >500 $\mu\text{mol/kg}$ to <20 $\mu\text{mol/kg}$ across the forearc (see compilations in
348 Wheat et al., 2018; Menzies et al., 2021). Similarly, K, Rb, Cs, and B are thought to be leached
349 from the subducted sediments and AOC once the slab has warmed to $T > 100\text{--}150^\circ\text{C}$ (Mottl et al.,
350 2004; Hulme et al., 2010). Concentrations of these in the serpentinite mud pore waters as a result
351 increase from shallow- to deep-sourced sites. Potassium changes from <1 mmol/kg to
352 >15 mmol/kg, Rb increases from <1 $\mu\text{mol/kg}$ to >5 $\mu\text{mol/kg}$, Cs from <5 nmol/kg to
353 >>50 nmol/kg, and B from <1 $\mu\text{mol/kg}$ to >3,000 $\mu\text{mol/kg}$ (Wheat et al., 2018). Contents of Si
354 are generally low in the serpentinite mud pore waters (Geilert et al., 2020) since Si is readily
355 taken up by the forearc mantle peridotite during serpentinization (e.g., Albers et al., 2020; Geilert
356 et al., 2021). But Si contents in slab-fluids were likely much higher shortly after their release, as
357 originating, for instance, from opal diagenesis and/or the transformation of smectite to illite (cf.,
358 e.g., Mottl et al., 2004; Kastner et al., 2014).

359 In the subduction channel, comminuted material as well as rock clasts react with these fluids.
360 Serpentinites, previously entitled “sponges” for fluid-mobile elements (Deschamps et al., 2011),
361 can contain high concentrations of Rb, Cs, B, and other fluid-mobile elements (e.g., Debret et al.,
362 2019; Albers et al., 2020). Contents of K_2O in the serpentinite clasts and mudflows are, however,
363 low with on average $\ll 0.1$ wt% (e.g., Savov et al., 2005a; Savov et al., 2005b)—despite the
364 general availability of K at the deeper-sourced mud volcanoes (see above). This is presumably the
365 case because serpentinite phases do not incorporate K in their structure. In consequence, the
366 forearc serpentinite does not act as a sink for K. Following this line of thought, K-containing
367 fluids are likely available to react with any lithology in the subduction channel that could form K-
368 bearing minerals. Such lithologies encompass subducted mafics, including OIB, which provide
369 the components and the chemical environment to form phengite or biotite.

370 The uptake of K has been mostly pervasive, as evidenced by the abundant replacement of former
371 groundmass by phengite in the recycled OIBs (Fig. 6 in Fryer et al., 2020) and the shortage of K-
372 bearing phases in metamorphic veins (Albers et al., 2019). Indeed, no such phases have been
373 observed in veins of OIBs recycled at Fantangisña. In addition, we generally observed less
374 phengite in the samples from Fantangisña and also little other K-bearing minerals so that it
375 remains somewhat enigmatic which phases account for the strong K_2O increase.

376 Likewise, the differences in metasomatic element uptake between the clasts from Fantangisña and
377 Asùt Tesoru (Fig. 4) are to some extent questionable and cannot unequivocally be clarified in this
378 study. The recycled OIB clasts from both sites should, theoretically, have experienced similar P/T

379 paths as well as interactions with similar slab-fluids when assuming (i) homogeneous
380 compositions of the incoming crust and (ii) similar exposure times to slab-fluids in the subduction
381 channel. But OIBs from Fantangisña, the shallower-sourced seamount, are marked by a net
382 increase in mass and uptake of K_2O , SiO_2 , MgO , and Na_2O and those from the deeper-sourced
383 Asùt Tesoru show increases in K_2O and SiO_2 and possibly losses of MgO and $Fe_2O_3^*$. Given
384 these distinctions, we follow that (i) and/or (ii) are incorrect. But even when considering
385 variations of the subducting lithosphere at the two sites (being >160 km apart) it is difficult to
386 explain the loss in MgO (and $Fe_2O_3^*$) in the Asùt Tesoru OIBs, since the subduction channel
387 mélange, the mud volcano conduits, and the mudflows in which the clasts resided are overall
388 characterized by ultramafic, Mg–Fe-rich materials. The second possibility would be that the
389 exposure times of the Asùt Tesoru samples within the Mg-rich environment were much shorter as
390 compared to the Fantangisña OIBs, but similar enrichments in K_2O between the two sites suggest
391 otherwise. In contrast, the addition of MgO (and maintenance of $Fe_2O_3^*$) in the samples from
392 Fantangisña appears plausible in this overall ultramafic environment; comparably, MgO contents
393 in seafloor basalt typically increase as a result of hydrothermal alteration and chlorite formation at
394 similar T (e.g., Staudigel et al., 1996; Bach et al., 2013). The gain in SiO_2 in samples from both
395 mud volcanoes presumably occurred in a pervasive manner—we assume that slab-fluids have
396 initially been siliceous (see above)—but may in addition be explained by the presence of silicates
397 in metamorphic veins: pectolite, prehnite, white mica, and lawsonite occur at both study sites
398 (Albers et al., 2019). Pectolite, $NaCa_2Si_3O_8(OH)$, however, appears to be more frequent in OIBs
399 from Fantangisña, which partly explains the Na_2O increase in these samples. Further, plagioclase
400 feldspar in these samples may be Na-rich as is typical for hydrothermally altered seafloor basalts
401 (Alt, 1995). Feldspar is predicted to be stable at rather low P/T along the $8^\circ C/km$ isotherm (Fig.
402 6b), which could indicate that it is part of the equilibrium assemblage in clasts from Fantangisña
403 but not in those from the deeper-sourced Asùt Tesoru. In the latter, the replacement of plagioclase
404 by lawsonite and phengite (see Fig. 6 in Fryer et al., 2020) lends further credence to this idea.
405 During this process, some of the Na from the plagioclase's albite component is possibly being
406 released from the rocks and hence explains the clasts' lower Na_2O contents. After all, aside from
407 heterogeneities in the composition of the subducting crust, it may be this and similar breakdown
408 reactions/changes in mineral stabilities that explain the variations between the OIBs from the two
409 mud volcanoes that tap different P/T conditions in the subduction channel.

410

411 4.1.3 Mariana forearc *P/T* conditions and ramifications of metasomatism for mineral 412 stabilities

413 The observed compositional changes have direct implications for the thermodynamic stability of
414 mineral phases. This is most striking for the stability field of phengite that is limited to <300°C in
415 unsubsucted OIB but, for the metasomatized ones, is increased to 600°C at both cold and warm
416 subduction zones (Fig. 5). In addition, besides this larger stability field, considerably larger
417 quantities of phengite (~6 instead of ~1.5 mol; Fig. 6) are being predicted for the metasomatized
418 OIBs.

419 The exact geotherm and the respective *P/T* conditions in the Mariana subduction system remain
420 vague. The depths to the slab below the mud volcanoes—from which *P* conditions can be
421 derived—could relatively well be determined using multi-channel seismic reflection data (e.g.,
422 Oakley et al., 2008). But estimates on *T* conditions are less precise because they chiefly rely on
423 interpretations of equilibrium mineral assemblages and mineral compositions in metamafic clasts
424 (e.g., Maekawa et al., 1993; Oakley, 2008), on across-forearc changes in pore water compositions
425 of the serpentinite mud (e.g., Mottl et al., 2004; Menzies et al., 2021), and on oxygen stable
426 isotope compositions of serpentine–magnetite pairs. The serpentine–magnetite pairs, for instance,
427 imply serpentinization *T* of up to 400°C for samples from Asùt Tesoru Seamount (Debret et al.,
428 2019), whereas metamafic mineral assemblages and compositions imply *T* of 200–250°C for that
429 seamount (Ichiyama et al., 2021). To make matters worse, the travel paths from depths to the
430 forearc seafloor are not completely understood; several authors have suggested that both
431 metamafic and serpentinite clasts may travel upwards in the subduction channel after having been
432 subducted to greater depths (e.g., Tamblyn et al., 2019) and before being entrained by mud
433 volcanism. They could hence have experienced metamorphic conditions greater than those right
434 below the individual mud volcanoes. In this sense, a blueschist clast from South Chamorro
435 Seamount was interpreted to have experienced up to 19 kbar and 590°C (Tamblyn et al., 2019).

436 Pressure at the slab is despite these uncertainties estimated at ~4 kbar below Fantangisña (~14 km
437 slab depth) and 6 kbar below Asùt Tesoru (~18 km; Oakley et al., 2008), with *T* of ~150°C and
438 250°C, respectively. Resultant geothermal gradients would span a range of 10–14°C/km, or even
439 6–17°C/km when including the *P/T* estimates for the other serpentinite mud volcanoes (see, e.g.,
440 Table 1 in Fryer et al., 2020). This large range may be explained by inaccuracies introduced by
441 several factors. For instance, the complex topography of the subducting Pacific Plate implies a
442 high relief of the slab–wedge interface (Fryer et al., 2020) and it is possible that topographic
443 highs such as subducted seamounts cause seismic reflections that are interpreted as the top of the
444 subducting slab; these may, however, protrude from the surrounding subducting seafloor by

445 several kilometers and hence affect the depth estimates. Temperature estimates on the other hand,
446 in particular the ones based on metamorphic mineral assemblages, may be biased by the time the
447 metamorphism occurred. Shortly after the subduction initiation in the Eocene, the mantle wedge
448 was much hotter than today, which lead to higher-grade metamorphism at a given depth of the
449 subduction channel than today (Ichiyama et al., 2021). In support of this, age-dating metamorphic
450 minerals in blueschist clasts from South Chamorro Seamount revealed formation ages of >45 Ma
451 (Tamblyn et al., 2019).

452 The geotherm of $\sim 8^\circ\text{C}/\text{km}$ appears to be best consistent when comparing the observed mineral
453 assemblages (Albers et al., 2019; Fryer et al., 2020; Deng et al., 2021; Ichiyama et al., 2021) with
454 our equilibrium assemblage diagrams (Fig. 5b). Along this geotherm, jadeitic pyroxene joins the
455 metamorphic assemblage at ~ 7 kbar/ 200°C (Fig. S3b), which would be the minimum P/T
456 conditions the clasts at Asùt Tesoru Seamount have experienced. The key criterion for the
457 $8^\circ\text{C}/\text{km}$ geotherm is the presence of lawsonite, which is not predicted for steeper geotherms, e.g.,
458 of $10^\circ\text{C}/\text{km}$ (dashed line in Fig. 5b). Following this argument, the lack of lawsonite in OIBs from
459 Fantangisña Seamount implies $P \leq 4$ kbar—which would further implicate $\sim 100^\circ\text{C}$ when
460 following the $8^\circ\text{C}/\text{km}$ geotherm. The T the OIBs experienced was, however, likely higher as
461 implied by the presence of pumpellyite that is restricted to $160\text{--}220^\circ\text{C}$. It must be kept in mind
462 though that the computed phase diagram applies to the recycled OIB's median composition. Due
463 to compositional differences between individual clasts and between Fantangisña and Asùt Tesoru,
464 (minor) deviations between the predicted and the observed mineral assemblages and their
465 compositions are not unlikely. For example, amphibole is predicted to be mainly glaucophane
466 above ~ 5.5 kbar/ 150°C , with a limited riebeckite component; lower MgO in the clasts from Asùt
467 Tesoru relative to those from Fantangisña (Fig. 3) would potentially decrease the glaucophane
468 fraction in amphibole. Allowing, during thermodynamic modeling, only for the formation of
469 amphibole with compositions similar to those observed by Ichiyama et al. (2021), i.e.,
470 $\text{Rbk}_{0.65}\text{Gln}_{0.35}$, results in a very similar mineral assemblage (Fig. S5). The amount of amphibole,
471 however, is lower in particular at intermediate P/T at which higher amounts of pyroxene are
472 instead predicted, and pumpellyite is stable up to somewhat higher P/T conditions. The predicted
473 pyroxene compositions (similar amounts of the aegirine and jadeite components; Fig. S6) are also
474 similar to those analyzed by Ichiyama et al. (2021). Further, the lower bulk Al_2O_3 in the OIBs
475 recycled at Fantangisña (median = 10.9 wt% vs. 16.0 wt% at Asùt Tesoru; Fig. 3) may explain
476 lower amounts of phengite (Albers et al., 2019; Ichiyama et al., 2021) in clasts from this mud
477 volcano, since Al is an important constituent in the muscovite component of phengite.

478 Aside from the compositional variability, the metasomatism of the clasts is a continual process:
479 they react with fluids with evolving solute loads (in response to increasing P/T conditions) while
480 being dragged to greater depths. Some of the metasomatism likely occurred at relatively late
481 stages, i.e., after the subduction to and metamorphism of the (at that time only partly
482 metasomatized) OIB clasts at a certain depth. As metamorphic reactions can be considered
483 generally rather sluggish at the considered P/T range, the clasts' equilibration with the ever-
484 evolving slab-fluid should lag behind and P and T overstepping may be needed for the reactions
485 to proceed (e.g., Pattison et al., 2011). This assumption is supported by the presence of vein
486 mineralogies in the metamafics that are distinct from the phase assemblages in the clast's
487 groundmasses. Sodic amphibole, pumpellyite, and chlorite for example replace Na pyroxene or
488 the igneous groundmass (Ichiyama et al., 2021) but have not been observed in veins that formed
489 in apparent equilibrium with the slab-derived fluids in the subduction channel (Albers et al.,
490 2019). Following this line of thought it would be possible that phases such as lawsonite formed in
491 the subducted OIB before the rocks were metasomatized to their current compositions.

492 Taken together, a reasonable consensus between observations and models exists. However,
493 reproducing the metamorphic phase assemblages by equilibrium modeling is impeded by
494 compositional variabilities, the timing of the metasomatism, and potentially by partial out-of-
495 equilibrium states of the clasts. We estimate the geothermal gradient at 8–10°C/km, whereby the
496 lower gradient appears realistic for today's mature subduction zone in which mantle wedge has
497 been cooled by the >180 My old subducting Pacific Plate since the Eocene. Metamorphism in the
498 geologic past may have occurred at higher T . Our model results hence strengthen previous studies
499 suggesting ~4 kbar/up to 160–220°C for the OIBs recycled via the Fantangisña mud volcano and
500 up to 7–8 kbar/200–350°C for those from Asùt Tesoru. The metasomatic changes in bulk
501 composition markedly increase the stability field of phengite.

502

503 **4.2 Reaction path modeling constraints on metasomatism at shallow depths**

504 We carried out thermodynamic reaction path modeling to better understand the fluid–rock
505 reactions in the subduction channel and the most obvious metasomatic changes, i.e., the transfer
506 of K_2O from the subducting slab into OIB. The models are thought to provide a generalized view
507 of mass transfer at subduction depths of 15–20 km.

508 Sediments being subducted at the Mariana Trench consist of chert, radiolarite, volcanic turbidites,
509 and pelagic clay, of which only the turbidites and clay contain significant amounts of K_2O (up to

510 ~1.9 wt% and 3.9 wt%, respectively; Plank & Langmuir, 1998). The limited thicknesses of these
511 units east of the Mariana Trench (190–220 m and 40–80 m, respectively; Plank et al., 2000)
512 restrict the overall amounts of K₂O that can be liberated from these. The other main source for
513 K₂O in the slab-derived fluids is subducting AOC. At a global scale, AOC has on average
514 0.65 wt% K₂O (Staudigel, 2014) but contents in the Cretaceous basalts east of the Mariana
515 Trench can exceed 5 wt% (ODP Site 801, the recovery of which does, however, not necessarily
516 represent ‘typical’ altered AOC as it contains a silicic hydrothermal deposit; Kelley et al., 2003).
517 The igneous basement is hundreds of meters thick, providing a vast reservoir for K₂O.

518 As starting compositions in the models, we used the bulk sediment composition from east of the
519 Mariana Trench, AOC (the conservative composition with 0.65 wt% K₂O), and a 50:50 mixture
520 of the two. The modeling consists of two steps: (i) to approximate the composition of the fluid
521 that is released from the slab, we equilibrated sediments, AOC, and the 50:50 mixture,
522 respectively, with a fluid at $P = 5$ kbar, varying T (150–400°C in 50°C steps), and a final
523 fluid/rock mass ratio (f/r ratio) of 0.1; (ii) to mimic fluid–rock reactions in the subduction
524 channel, we reacted a median NW Pacific OIB composition (Tab. 2) with the fluid resulting from
525 (i), at $P = 5$ kbar, $T = 200$ and 300°C, and a final f/r ratio of 10. Details on the models and
526 thermodynamic data are provided in the Supplementary Information.

527 Modeling results of the AOC–OIB runs are summarized in Figure 7; results from the other setups
528 are presented in Figure S7. In all cases, K as well as Si, Ca, and Na are mobilized from the
529 starting lithologies (Figs. 7a & S7a). Solute concentrations in the fluids are, however, strongly
530 dependent on T and partly dependent on the f/r ratio; concentrations can vary by a factor of ten
531 and more. The corresponding mineral assemblages predicted for the subducted slab are shown in
532 Figure S8. Upon the reaction of the solute-laden fluids with OIB, mineral assemblages are
533 dominated by epidote, phengite, and chlorite at 200°C with abundant lawsonite at fluid-
534 dominated and quartz at more rock-dominated conditions when the fluid is (partly) sourced in
535 subducting sediment (Figs. 7b & S7b). At 300°C, plagioclase, epidote, and phlogopite
536 characterize the equilibrium assemblage in the model runs following AOC and AOC–sediment
537 equilibration, with minor hematite, chlorite, and phengite at high f/r ratios. By contrast, the
538 sediment–OIB models predict dominantly quartz and garnet together with talc and stilpnomelane
539 (at high f/r ratios) and chlorite (towards lower f/r ratios). Bulk K₂O contents in the now
540 metasomatized OIBs have approximately doubled over most of the model conditions at 200°C,
541 now exceeding 2 wt% except for strongly fluid-dominated systems and towards completed
542 reaction in the sediment–OIB runs (Figs. 7c & S7c). At 300°C, K₂O even approaches 3 wt.% in

543 the AOC–OIB models whereas a loss of K₂O from the OIB is predicted for the sediment–OIB
544 models. The major hosts of K₂O are phengite and phlogopite at 200°C and 300°C, respectively.

545 Our modeled fluid compositions are generally consistent with observations from the serpentinite
546 mud volcanoes in that they imply considerable mobilization of mass from the slab at shallow
547 depths and low *T*. The fluids in the Mariana forearc, however, undergo severe compositional
548 changes during the reaction with solids in the subduction channel and during their rise to the
549 forearc seafloor (e.g., loss of Si and Ca; see Section 4.1.2), so that the modeled fluid compositions
550 cannot directly mirror those recorded in the serpentinite mud pore waters. But, for instance, the
551 presence of abundant prehnite and pectolite with equilibrium growth structures in metamorphic
552 veins in the recycled OIBs (Albers et al., 2019) lends strong credence to the existence of Si–Ca–
553 Na–K-containing fluids. Further, the corresponding phase assemblages in the fluid source
554 lithologies (Fig. S8) appear reasonable for the physicochemical (modeling) conditions:
555 comparable assemblages were described as alteration products in mafic rocks and/or sediments
556 that experienced metamorphism up to blueschist grade overprints (e.g., Ernst, 1984; Jayko et al.,
557 1986). Phases predicted to be stable in the metasomatized OIB (Figs. 7c & S7c) resemble those in
558 metabasaltic rocks that were interpreted to have reacted with slab-derived fluids at shallow
559 subduction levels, such as greenstones and blueschists from the Franciscan Complex (e.g., Bebout
560 & Barton, 1993; Ukar & Cloos, 2014).

561 It must be kept in mind, however, that our models oversimplify the natural system by assuming
562 complete chemical equilibrium between all reactants, by not including kinetic effects, as well as
563 by limitations of thermodynamic data at low *T* and a possible shortage of relevant low-*T* mineral
564 phases in the database. The models cannot emulate the vast complexity of natural reactions taking
565 place in subduction zones, which are influenced by factors such as the physicochemical
566 conditions during dehydration (*T* and *f/r* ratios), heterogeneities in type, composition, and
567 alteration of subducting lithologies. For example, Staudigel et al. (2010) speculated that
568 volcanoclastic sediments, providing the greatest share of K as sedimentary input to the Mariana
569 subduction zone, should be particularly predominant close to large seamounts; following the
570 arguments in Mottl et al. (2004), it is very likely that K will be released from the slab, especially
571 from volcanic turbidites, presumably even at *T* lower than those in our models. The average
572 composition of subducting sediments used as input in our models will not take account of such
573 variations. In addition, we also did not consider interactions between the different lithologies in
574 the subduction channel, e.g., between ultramafic material and OIB, which would have added
575 further complexity. More dedicated modeling and possibly experimental work would be needed
576 to better reflect those natural fluid–rock interactions.

577 The key observations are, however, that at shallow subduction conditions (i) the release of K-
578 containing fluids from subducting sediments and from AOC as well as (ii) the uptake of K₂O by
579 OIB, i.e., K₂O-metasomatism, are thermodynamically plausible, and (iii) that this may lead to the
580 formation of substantial amounts of phengite or other K-bearing phases. The models, in addition,
581 imply K and other solutes such as Si, Ca, and Na to be elevated in slab-derived fluids at
582 convergence margins across a range of thermal conditions, i.e., at both cool and warm subduction
583 settings. The results hence strongly support the feasibility of metasomatic changes of (mafic)
584 materials to occur in subduction channels at depths \ll 30 km.

585

586 **4.3 Implications of shallow metasomatism and the role of phengite in element cycling**

587 Following the results from this study and from the research conducted at the Mariana forearc over
588 several decades, it has become clear that incoming lithologies must considerably change their
589 composition at forearc depths. Independent of uncertainties in peak metamorphic conditions, this
590 shallow transfer and redistribution of mass potentially has profound implications for processes at
591 deeper subduction levels. The shallow removal of certain elements from the subducting
592 lithosphere affects the compositions of rocks that are subducted to beyond-forearc depths.
593 Likewise, the mobilized elements impact fluid–rock reactions in the subduction channel and the
594 mantle wedge. Low- to intermediate-grade metamorphic/metasomatic phases formed here, such
595 as lawsonite and phengite (Figs. 5 & 6), will transport H₂O and elements to greater depths. Both
596 minerals have extensive stability fields up to depths of >200 km (e.g., Poli & Schmidt, 1995;
597 Schmidt, 1996). Phengite contains about 4 wt% H₂O and 12 wt% K₂O and is considered as an
598 important carrier for these to and beyond sub-arc depths.

599 It is hence questionable whether K₂O and H₂O captured in phengite will ultimately be available to
600 contribute to arc magmatism (also see discussion on phengite breakdown in, e.g., Chen et al.,
601 2018). Our study demonstrates that the amount of phengite in individual metamafic rock clasts
602 can (theoretically) be quite large. It cannot, however, be estimated how much phengite overall is
603 formed during such processes in other subduction systems. But seamounts depict substantial
604 topographic irregularities on subducting oceanic plates and contribute to relief within the
605 subduction channel, and it is well recognized that seamounts on outer-trench rises are deformed
606 by faulting as the plate bends prior to subduction (e.g., Fryer & Smoot, 1985; Zhou & Lin, 2018).
607 Subducting seamounts are subject to local increases in fluid pore pressure as they move through
608 the subduction channel (e.g., Bell et al., 2010) and thus are prone to (further) deformation and
609 possible decapitation (Watts et al., 2010). Although the detailed fate of deformation remains

610 unclear (e.g., Wang & Bilek, 2014), it appears likely that much eroded material from subducted
611 seamounts will be available for fluid–rock reactions (and fluid-induced metasomatism) in
612 subduction channels/mélanges. With subduction channel thicknesses typically ranging from
613 hundreds of meters to several kilometers (e.g., Cloos & Shreve, 1988; Guillot et al., 2009;
614 Vannucchi et al., 2012) and the vast number of (eventually subducting) seamounts worldwide, it
615 becomes clear that large masses of rock are likely to be compositionally (and mineralogically)
616 modified. Bearing in mind the wide stability field of phengite (Fig. 5b), we suppose that phengite
617 formation in metamafics is potentially widespread throughout both cold and warm subduction
618 zones.

619 Aside from being one of the major hosts for K in subduction environments, phengite is also
620 known to incorporate high contents of fluid-mobile trace elements (e.g., Busigny et al., 2003;
621 Bebout et al., 2013; Sievers et al., 2016). Studies on high-*P* minerals in eclogitic rocks from the
622 Central Alps have shown that phengite can accommodate >90% of the whole-rock budget of Rb,
623 Cs, and Ba (Zack et al., 2001). Determining the trace elemental distribution within the recycled
624 OIBs is beyond the scope of this study, but bulk rock data imply enrichments in Rb, Cs, and to a
625 lesser degree Th, as well as markedly lower Sr and Ba contents when compared to unsubducted
626 Pacific seamounts (Fig. 8). The losses in Sr and Ba can be explained by the breakdown of Ca
627 plagioclase and/or of clays during the subduction of the OIB (e.g., Putnis & John, 2010; Alt &
628 Teagle, 2003). Gains in Rb and Cs can putatively—as those in K₂O and SiO₂—be ascribed to
629 metasomatism in the subduction channel. Indeed, previous studies have shown that these
630 elements are mobilized in the Mariana forearc and concentrations in the slab-fluids are high (e.g.,
631 Wheat et al., 2018; Albers et al., 2020). We speculate that much of the Rb and Cs is hosted by
632 phengite. This interpretation is in accordance with considerably higher amounts of Rb and Cs at
633 Asùt Tesoru, relative to Fantangisña Seamount, from which phengite has primarily been reported
634 (Ichiyama et al., 2021). Similarly, phengite in blueschist clasts from the South Chamorro
635 Seamount, which has a similar depth-to-slab as Asùt Tesoru, has been shown to be the major
636 carrier of slab-released fluid-mobile elements (B, Li, and Be; Pabst et al., 2012). The observed
637 fluid-metasomatism, resulting in enhanced phengite formation, thus also directly influences trace
638 element budgets.

639 Would such an increased formation of phengite have a bearing on the importance of phlogopite,
640 the K–Mg mica that was suggested to play a major role in the cycling of K₂O and H₂O?
641 Phlogopite crystallizes in the mantle wedge as a consequence of the infiltration of K-enriched
642 slab-derived fluids, and it decomposes at deeper levels where it releases H₂O that in turn triggers
643 mantle wedge partial melting and hence contributes to back-arc magmatism (e.g., Peacock, 1990;

644 Sudo & Tatsumi, 1990). The phlogopite breakdown reactions also release K_2O , generating K-rich
645 magmas (e.g., Foley & Peccerillo, 1992; Condamine & Médard, 2014). However, in the Izu–
646 Bonin back-arc, Tamura et al. (2007) suggested that it is the breakdown of phengite that causes an
647 increased mobility of K and consequently K-rich magmatism—whereas they attributed the
648 scarcity of K-rich magmas in the arc-front to the presence and stability of phengite in the slab.
649 And also other authors pointed out that phlogopite is not needed to generate K-rich melts (e.g.,
650 Wang et al., 2017). Our study highlights the complexity of the subduction channel’s mineralogy,
651 which cannot be precisely defined. Potassium that is incorporated into phengite at shallow depths
652 will unlikely be available to infiltrate the mantle wedge (to form phlogopite) somewhat deeper in
653 the system. It remains unclear how much of the slab-released K is trapped in the subduction
654 channel and how much of it can rise into/through the mantle wedge. Yet, at least at the forearc of
655 the Mariana subduction zone, K-enriched fluids expelled at the serpentinite mud volcanoes
656 provide evidence that the amount of K released from the slab outweighs that incorporated at
657 depths. The formation of phlogopite deeper within the Mariana subduction system hence appears
658 plausible. Indeed, incompatible trace element abundances and isotopic compositions of primitive
659 magmas from the Mariana arc imply the presence of phlogopite in the source region (e.g., Tamura
660 et al., 2014).

661 Conclusively, our geochemical data and thermodynamic models imply that elements are
662 mobilized and redistributed soon after the subduction of sediments and AOC at the Mariana
663 convergent margin. This redistribution of mass from phases that are only stable at low P/T into
664 metamorphic/metasomatic minerals such as phengite and/or lawsonite, both stable until great
665 depths, will affect geochemical cycling of major and trace elements deep within subduction
666 zones. We have conceptualized these processes in Figure 9.

667 In the literature, contrasting reports persist on the degree of element mobility in shallow
668 subduction settings. For example, Bebout & Barton (1993) reported on blueschist metabasaltic
669 rocks from the Catalina Schist (Catalina Island, California) that exhibit K_2O enrichments up to >4
670 wt.%, accompanied by enrichments of Cs and Ba. Sievers et al. (2016) provided evidence for the
671 replacement of plagioclase by phengite in metadiorites and metagabbros, also from the Catalina
672 Schist, and corresponding enrichments in K_2O and fluid-mobile trace elements. However,
673 occurrences of exhumed blueschists (and also eclogites) with strongly elevated K_2O contents are
674 rare. This is surprising considering that large amounts of K subduct as clays in pelagic sediment
675 and AOC and the tendency of K to be released into the fluid phase at shallow subduction
676 conditions (see, e.g., discussion in Kastner et al., 2014), i.e., the principal availability of K to
677 interact with materials in the subduction channel. Despite that, Shervais et al. (2011) documented

678 prehnite–pumpellyite facies metavolcanics in a serpentinite mélange (Tehama–Colusa mélange,
679 Coast Ranges, California) that are enriched in SiO₂ and Na₂O, but not K₂O. Ghatak et al. (2012)
680 even demonstrated that metaafic rocks that experienced up to eclogite metamorphism (Feather
681 River ultramafic belt, Coast Ranges, California) largely preserved their protolith major and trace
682 elemental compositions except for some fluid-mobile elements such as Ba, Pb, and to a smaller
683 extent La, U, and Sr. More generally, Harlov & Austrheim (2013) summarized that subducting
684 sediments and probably also igneous crustal rocks can largely retain their inventories of even the
685 more fluid-mobile elements to at least 90 km in relatively cool subduction zones; higher
686 geothermal gradients may generate greater forearc devolatilization leading to greater loss of fluids
687 and fluid-mobile elements to the mantle wedge. They further stated that, at forearc depths, only
688 the extremely mobile elements (for instance B, Cs, As, and Sb for the blueschist metasedimentary
689 suite of the Catalina Schist) show a clear record of whole-rock loss, as based on comparisons
690 between higher-grade rocks with lower-grade or unmetamorphosed equivalents.

691 A number of factors may influence the liberation of elements as well as metasomatic processes
692 occurring soon after subduction, including the composition and state of the incoming lithosphere
693 (i.e., type and thickness of sediment, nature and degree of alteration of the oceanic basement) or
694 the thermal structure of the system. The variety of these in subduction zones worldwide likely
695 leads to decreased element mobility in some and elevated mobility in other sites. Further, the
696 position of subducting rock within the convergent margin—it could metamorphose/metasomatize
697 as part of the intact volcanic basement, could be positioned in the vicinity of a fluid conduit, or
698 float within the subduction channel—is an important additional factor that contributes to the
699 variability of element mobility (see discussion and references in Spandler & Pirard, 2013). Within
700 the intact basement, rocks potentially mostly dehydrate at low *f/r* ratios and are being depleted in
701 fluid-mobile elements (that are, once released, transported towards the upper plate). Since the
702 subducting lithosphere provides a vast reservoir, large amounts of fluids and elements will be
703 mobilized even though the elemental losses in individual portions of rock may appear minor and
704 imply subduction metamorphism in a (more or less) closed system. Rocks situated along fluid
705 pathways or in the subduction channel mélange, however, interact with slab-fluids at higher *f/r*
706 ratios, leading to more increased modifications.

707 In the Mariana forearc, the extensive fluid–rock reactions in the subduction channel are
708 particularly well documented. Enrichments (or depletions) of certain elements in rock clasts (this
709 study; see also, e.g., Johnson, et al., 2014; Kahl et al., 2015; Tamblyn et al., 2019; Albers et al.,
710 2020) allowed reconstructing processes in the subducting slab and during the fluids’ rise toward
711 the forearc seafloor. Serpentinites, for instance, incorporate fluid-mobile elements (Wei et al.,

712 2005; Savov et al., 2007; Debret et al., 2019). Yet, despite high concentrations of these in the
713 rocks, fluids emanating at the mud volcano summits still are considerably enriched in the same
714 elements, implying that the mobilized amounts of these exceed what serpentinites can take up.
715 Considering the putatively vast volumes of serpentinite produced in the Mariana forearc (e.g., Cai
716 et al., 2018), the amount of mass mobilized from the slab must be immense. Research at the
717 serpentinite mud volcanoes has clearly pointed out the significance of the liberation and transfer
718 of fluids and mass at subduction depths <30 km. In line with these results, Kastner et al. (2014)
719 estimated the global return flux of fluids and solutes from forearcs to the ocean through seeps and
720 fault-controlled conduits to be large enough to importantly impact seawater chemistry (such as
721 Mg, Ca, or SO₄).

722 Mass transfer and associated metasomatic processes that set in at shallow forearc depths are,
723 however, often overlooked when geochemical cycling in subduction zones is investigated. Many
724 (modeling) studies, for example, compare subduction inputs to arc volcanic outputs without
725 considering metasomatism-related phase transitions. Our results strongly suggest that, for a
726 holistic view, these processes need to be integrated. In line with these implications, previous
727 studies concluded that up to kilometer-thick *mélange* zones in the subduction channel (formed
728 during the mechanical mixing of materials from the subducting and overriding plates) may
729 ultimately control the nature and composition of slab-derived fluids that enter the mantle wedge
730 (e.g., King et al., 2006; Marschall & Schumacher, 2012; see also Spandler & Pirard, 2013).

731

732 **5 Summary and conclusions**

733 Data and models presented here provide unique insight regarding fluid-induced mass transfer and
734 metasomatism within the shallow depths of an active subduction zone. We demonstrate that
735 subducted OIB clasts have undergone substantial compositional changes, most likely at
736 conditions that did not largely exceed 7–8 kbar and 200–350°C. Most noticeable and consistent
737 throughout all clasts are enrichments in K₂O and H₂O, accompanied by SiO₂, Na₂O, and MgO
738 gains in samples from Fantangisña Seamount and SiO₂ gains but MgO and Fe₂O₃* losses in
739 samples from Asùt Tesoru Seamount. In addition, the fluid-mobile elements Cs and Rb are
740 increased whereas Ba and Sr contents are decreased in all samples.

741 The metasomatic changes can be explained by the interaction of element-laden, slab-derived
742 fluids with (fragmented) parts of subducted seamounts in the subduction channel. Our reaction
743 path models predict the release of fluids enriched in K and other solutes from subducting oceanic

744 lithosphere even at $T < 200^{\circ}\text{C}$, consistent with known compositions of slab-derived fluids at the
745 Mariana forearc seafloor. A K_2O -increase in OIB during its reaction with the above fluid is
746 thermodynamically feasible.

747 The observed changes in major element composition have considerable ramifications for the
748 clasts' metamorphic phase assemblages. Our equilibrium assemblage diagrams predict a
749 strikingly increased stability field and much greater absolute amounts of phengite (up to four
750 times as much) relative to unmetasomatized OIB. Phengite in turn can carry K_2O , H_2O , and fluid-
751 mobile trace elements beyond sub-arc depths.

752 These results highlight the importance of acknowledging subduction processes at shallow depths
753 (< 30 km) as they may play a fundamental role in controlling *which* components as well as *in*
754 *which state* (i.e., bound in which minerals) these components ultimately reach greater depths
755 where they may or may not contribute to arc magmatism. We suggest that metasomatic/rock
756 transformation processes likely take place shallow within all subduction zones, and that these
757 processes could affect all subducted rock types including sediments, MORB, and OIB as well as
758 the base of the mantle wedge.

759

760 **6 Conflict of Interest**

761 The authors declare that the research was conducted in the absence of any commercial or
762 financial relationships that could be construed as a potential conflict of interest.

763

764 **7 Author Contributions**

765 EA, JS, YI, and PF sailed IODP Exp. 366. EA planned and designed the study. YI and EA
766 examined the samples petrographically; bulk rock analyses were conducted by JS. EA performed
767 thermodynamic calculations; CTH and EA compiled the thermodynamic database for EQ3/6. The
768 manuscript was written by EA with contributions of all co-authors.

769

770 **8 Funding**

771 EA acknowledges funding by the Special Priority Program 527 'International Ocean Discovery
772 Program' of the German Research Foundation (DFG), grant BA 1605/18–1, and by the Helmholtz

773 Association ‘POSY – The Polar System and its Effects on the Ocean Floor’ (project no. ExNet-
774 0001-Phase2-3). PF acknowledges funding by IODP-US Science Support Program. This is HIGP
775 contribution #

776

777 **9 Acknowledgments**

778 This research used samples and data provided by IODP. We are grateful to the captain and crew
779 of the D/V JOIDES Resolution, to the IODP science technicians, and to the Exp. 366 Science
780 Party. We greatly appreciate editorial handling by Philipp A. Brandl and constructive reviews by
781 Jeffrey Alt and one anonymous reviewer. The processing charges for this open-access article were
782 covered by the University of Bremen. A preprint of this article has been uploaded to EarthArXiv
783 and is available at <https://doi.org/10.31223/x56d1s>.

784

785 **10 References**

786 Albers, E.; Bach, W.; Klein, F.; Menzies, C. D.; Lucassen, F. & Teagle, D. A. H., 2019, Fluid–
787 rock interactions in the shallow Mariana forearc: carbon cycling and redox conditions, *Solid*
788 *Earth*, 10, 907–930, doi:10.5194/se-10-907-2019

789 Albers, E.; Kahl, W.-A.; Beyer, L. & Bach, W., 2020, Variant across-forearc compositions of
790 slab-fluids recorded by serpentinites: implications on the mobilization of FMEs from an active
791 subduction zone (Mariana forearc), *Lithos*, 364–365, 105525, doi:10.1016/j.lithos.2020.105525

792 Alt, J. C., 1995, Subseafloor processes in mid-ocean ridge hydrothermal systems, *Geophys.*
793 *Monogr. Ser.*, 91, 85–114, doi:10.1029/gm091p0085

794 Alt, J. C. & Teagle, D. A. H., 2003, Hydrothermal alteration of upper oceanic crust formed at a
795 fast-spreading ridge: mineral, chemical, and isotopic evidence from ODP Site 801, *Chem. Geol.*,
796 201, 191–211, doi:10.1016/S0009-2541(03)00201-8

797 Bach, W.; Jöns, N. & Klein, F., 2013, Metasomatism within the ocean crust, in: Harlov, D. E. &
798 Austrheim, H. (eds.) Metasomatism and the chemical transformation of rock, Lecture notes in
799 Earth system sciences, Springer, Berlin, Heidelberg, doi:10.1007/978-3-642-28394-9_8

800 Baker, P. E.; Castillo, P. R. & Condliffe, E., 1995, Petrology and geochemistry of igneous rocks
801 from Allison and Resolution Guyots, Sites 865 and 866, in: Winterer, E. L., Sager, W. W., Firth,

- 802 J. V. & Sinton, J. M. (eds.), Proc. ODP., Sci. Results, 143: College Station, TX (Ocean Drilling
803 Program), doi:10.2973/odp.proc.sr.143.216.1995
- 804 Baldwin J. A.; Powell, R.; Brown, M.; Moraes, R. & Fuck, R. A., 2005, Modelling of mineral
805 equilibria in ultrahigh-temperature metamorphic rocks from the Anapolis–Itaucu Complex,
806 central Brazil, *J. Metamorph. Geol.*, 23, 511–531, doi:10.1111/j.1525-1314.2005.00591.x
- 807 Bebout, G. E. & Barton, M. D., 1993, Metasomatism during subduction: products and possible
808 paths in the Catalina Schist, California, *Chem. Geol.*, 108, 61–92, doi:10.1016/0009-
809 2541(93)90318-d
- 810 Bebout, G. E.; Ryan, J. G.; Leeman, W. P. & Bebout, A. E., 1999, Fractionation of trace elements
811 by subduction-zone metamorphism—effect of convergent-margin thermal evolution, *Earth
812 Planet. Sci. Lett.*, 171, 63–81, doi:10.1016/s0012-821x(99)00135-1
- 813 Bebout, G. E.; Agard, P.; Kobayashi, K.; Moriguti, T. & Nakamura, E., 2013, Devolatilization
814 history and trace element mobility in deeply subducted sedimentary rocks: evidence from
815 Western Alps HP/UHP suites, *Chem. Geol.*, 342, 1–20, doi:10.1016/j.chemgeo.2013.01.009
- 816 Bekins, B.; McCaffrey, A. M. & Dreiss, S. J., 1994, Influence of kinetics on the smectite to illite
817 transition in the Barbados accretionary prism, *J. Geophys. Res. Solid Earth*, 99, 18147–18158,
818 doi:10.1029/94jb01187
- 819 Bell, R.; Sutherland, R.; Barker, D. H. N.; Henrys, S.; Bannister, S.; Wallace, L. & Beavan, J.,
820 2010, Seismic reflection character of the Hikurangi subduction interface, New Zealand, in the
821 region of repeated Gisborne slow slip events, *Geophys. J. Int.*, 180, 34–48, doi:10.1111/j.1365-
822 246x.2009.04401.x
- 823 Busigny, V.; Cartigny, P.; Philippot, P.; Ader, M. & Javoy, M., 2003, Massive recycling of
824 nitrogen and other fluid-mobile elements (K, Rb, Cs, H) in a cold slab environment: evidence
825 from HP to UHP oceanic metasediments of the Schistes Lustrés nappe (western Alps, Europe),
826 *Earth Planet. Sci. Lett.*, 215, 27–42, doi:10.1016/s0012-821x(03)00453-9
- 827 Cai, C.; Wiens, D. A.; Shen, W. & Eimer, M., 2018, Water input into the Mariana subduction
828 zone estimated from ocean-bottom seismic data, *Nature*, 563, 389–392, doi:10.1038/s41586-018-
829 0655-4

- 830 Chen, S.; Guo, X.; Yoshino, T.; Jin, Z. & Li, P., 2018, Dehydration of phengite inferred by
831 electrical conductivity measurements: implication for the high conductivity anomalies relevant to
832 the subduction zones, *Geology*, 46, 11–14, doi:10.1130/g39716.1
- 833 Cloos, M. & Shreve, R. L., 1988, Subduction-channel model of prism accretion, mélange
834 formation, sediment subduction, and subduction erosion at convergent plate margins: 1.
835 Background and description, *Pure Appl. Geophys.*, 128, 455–500, doi: 10.1007/bf00874548
- 836 Codillo, E. A.; Le Roux, V. & Marschall, H. R., 2018, Arc-like magmas generated by mélange-
837 peridotite interaction in the mantle wedge, *Nat. Commun.*, 9, 2864, doi:10.1038/s41467-018-
838 05313-2
- 839 Condamine, P. & Médard, E., 2014, Experimental melting of phlogopite-bearing mantle at 1 GPa:
840 implications for potassic magmatism, *Earth Planet. Sci. Lett.*, 397, 80–92,
841 doi:10.1016/j.epsl.2014.04.027
- 842 Davis, A. S.; Pringle, M. S.; Pickthorn, L.-B. G. & Clague, D. A., 1989, Petrology and age of
843 alkalic lava from the Ratak Chain of the Marshall Islands, *J. Geophys. Res.*, 94, 5757–5774,
844 doi:10.1029/jb094ib05p05757
- 845 de Capitani, C. & Brown, T. H., 1987, The computation of chemical equilibrium in complex
846 systems containing non-ideal solutions, *Geochim. Cosmochim. Acta*, 51, 2639–2652,
847 doi:10.1016/0016-7037(87)90145-1
- 848 de Capitani, C. & Petrakakis, K., 2010, The computation of equilibrium assemblage diagrams
849 with Theriak/Domino software, *Am. Mineral.*, 95, 1006–1016, doi:10.2138/am.2010.3354
- 850 Debret, B.; Albers, E.; Walter, B.; Price, R.; Barnes, J. D.; Beunon, H.; Facq, S.; Gillikin, D. P.;
851 Mattielli, N. & Williams, H., 2019, Shallow forearc mantle dynamics and geochemistry: new
852 insights from IODP Expedition 366, *Lithos*, 326–327, 230–245, doi:10.1016/j.lithos.2018.10.038
- 853 Deng, J.; Zhang, L.; Liu, H.; Liu, H.; Liao, R.; Mastoi, A. S.; Yang, X. & Sun, W., 2021,
854 Geochemistry of subducted metabasites from the Mariana forearc: implications for Pacific
855 seamount subduction, *Geosci. Front.*, 12, 101117, doi:10.1016/j.gsf.2020.12.002
- 856 Deschamps, F.; Guillot, S.; Godard, M.; Andreani, M. & Hattori, K., 2011, Serpentinites act as
857 sponges for fluid-mobile elements in abyssal and subduction zone environments, *Terra Nova*, 23,
858 171–178, doi:10.1111/j.1365-3121.2011.00995.x

- 859 Ernst, W. G., 1984, Californian blueschists, subduction, and the significance of
860 tectonostratigraphic terranes, *Geology*, 12, 436–440, doi:10.1130/0091-
861 7613(1984)12<436:cbsats>2.0.co;2
- 862 Foley, S. & Peccerillo, A., 1992, Potassic and ultrapotassic magmas and their origin, *Lithos*, 28,
863 181–185, doi:10.1016/0024-4937(92)90005-j
- 864 Fryer, P. B., 2012, Serpentinite mud volcanism: observations, processes, and implications, *Ann.*
865 *Rev. Mar. Sci.*, 4, 345–373, doi:10.1146/annurev-marine-120710-100922
- 866 Fryer, P. & Smoot, N. C., 1985, Processes of seamount subduction in the Mariana and Izu-Bonin
867 Trenches, *Marine Geology*, 64, 77–90, doi:10.1016/0025-3227(85)90161-6
- 868 Fryer, P.; Ambos, E. L. & Hussong, D. M., 1985, Origin and emplacement of Mariana forearc
869 seamounts, *Geology*, 13, 774–777, doi:10.1130/0091-7613(1985)13<774:oaomf>2.0.co;2
- 870 Fryer, P., Pearce, J. A., Stokking, L. B., et al., 1992, Proc. ODP, Sci. Results, 125: College
871 Station, TX (Ocean Drilling Program), doi:10.2973/odp.proc.sr.125.1992
- 872 Fryer, P.; Mottl, M.; Johnson, L.; Haggerty, J.; Phipps, S. & Maekawa, H., 1995, Serpentine
873 bodies in the forearcs of western Pacific convergent margins: origin and associated fluids,
874 *Geophys. Monogr. Ser.*, 88, 259–279, doi:10.1029/gm088p0259
- 875 Fryer, P.; Gharib, J.; Ross, K.; Savov, I. & Mottl, M. J., 2006, Variability in serpentinite mudflow
876 mechanisms and sources: ODP drilling results on Mariana forearc seamounts, *Geochem.*
877 *Geophys. Geosyst.*, 7, Q08014, doi:10.1029/2005gc001201
- 878 Fryer, P.; Wheat, C. G.; Williams, T. & the Expedition 366 Scientists, 2018, Mariana convergent
879 margin and South Chamorro Seamount, Proc. IODP, 366: College Station, TX (International
880 Ocean Discovery Program), doi:10.14379/iodp.proc.366.101.2018
- 881 Fryer, P.; Wheat, C.; Williams, T.; Kelley, C.; Johnson, K.; Ryan, J.; Kurz, W.; Shervais, J.;
882 Albers, E.; Bekins, B.; Debret, B.; Deng, J.; Dong, Y.; Eickenbusch, P.; Frery, E.; Ichiyama, Y.;
883 Johnston, R.; Kevorkian, R.; Magalhaes, V.; Mantovanelli, S.; Menapace, W.; Menzies, C.;
884 Michibayashi, K.; Moyer, C.; Mullane, K.; Park, J.-W.; Price, R.; Sissman, O.; Suzuki, S.; Takai,
885 K.; Walter, B.; Zhang, R.; Amon, D.; Glickson, D. & Pomponi, S., 2020, Mariana serpentinite
886 mud volcanism exhumes subducted seamount materials: implications for the origin of life, *Phil.*
887 *Trans. R. Soc. A*, 378, 20180425, doi:10.1098/rsta.2018.0425

- 888 Geilert, S.; Grasse, P.; Wallmann, K.; Liebetrau, V. & Menzies, C. D., 2020, Serpentine alteration
889 as source of high dissolved silicon and elevated $\delta^{30}\text{Si}$ values to the marine Si cycle, *Nat.*
890 *Commun.*, 11, 5123, doi:10.1038/s41467-020-18804-y
- 891 Geilert, S.; Albers, E.; Frick, D. A.; Hansen, C. T. & von Blanckenburg, F., 2021, Systematic
892 changes in serpentine Si isotope signatures across the Mariana forearc – a new proxy for slab
893 dehydration processes, *Earth Planet. Sci. Lett.*, 575, 117193, doi:10.1016/j.epsl.2021.117193
- 894 Ghatak, A.; Basu, A. R. & Wakabayashi, J., 2012, Elemental mobility in subduction
895 metamorphism: insight from metamorphic rocks of the Franciscan Complex and the Feather
896 River ultramafic belt, California, *Int. Geol. Rev.*, 54, 654–685,
897 doi:10.1080/00206814.2011.567087
- 898 Giaramita, M.; MacPherson, G. J. & Phipps, S. P., 1988, Petrologically diverse basalts from a
899 fossil oceanic forearc in California: the Llanada and Black Mountain remnants of the Coast Range
900 ophiolite, *Geol. Soc. Am. Bull.*, 110, 553–571, doi:10.1130/0016-
901 7606(1998)110<0553:pdbfaf>2.3.co;2
- 902 Grant, J. A., 1986, The isocon diagram—a simple solution to Gresens' equation for metasomatic
903 alteration, *Econ. Geol.*, 81, 1976–1982, doi:10.2113/gsecongeo.81.8.1976
- 904 Gresens, R. L., 1967, Composition–volume relationships of metasomatism, *Chem. Geol.*, 2, 47–
905 65, doi:10.1016/0009-2541(67)90004-6
- 906 Guillot, S.; Hattori, K.; Agard, P.; Schwarz, S. & Vidal, O., 2009, Exhumation processes in
907 oceanic and continental subduction contexts: a review, in: Lallemand, S. & Funiciello, F. (eds.)
908 *Subduction zone geodynamics*, Springer, Berlin Heidelberg, doi:10.1007/978-3-540-87974-9
- 909 Harlov, D. E. & Austrheim, H., 2013, Metasomatism and the chemical transformation of rock: the
910 role of fluids in terrestrial and extraterrestrial processes, *Springer*, Berlin/Heidelberg,
911 doi:10.1007/978-3-642-28394-9
- 912 Holland, T. J. B. & Powell, R., 1998, An internally consistent thermodynamic dataset for phases
913 of petrological interest, *J. Metamorph. Geol.*, 16, 309–343, doi:10.1111/j.1525-
914 1314.1998.00140.x
- 915 Holland, T. J. B. & Powell, R., 2003, Activity-composition relations for phases in petrological
916 calculations: an asymmetric multicomponent formulation, *Contrib. Mineral. Petrol.*, 145, 492–
917 501, doi:10.1007/s00410-003-0464-z

- 918 Holland, T. J. B. & Powell, R., 2011, An improved and extended internally consistent
919 thermodynamic dataset for phases of petrological interest, involving a new equation of state for
920 solids, *J. Metamorph. Geol.*, 29, 333–383, doi:10.1111/j.1525-1314.2010.00923.x
- 921 Hulme, S. M.; Wheat, C. G.; Fryer, P. B. & Mottl, M. J., 2010, Pore water chemistry of the
922 Mariana serpentinite mud volcanoes: a window to the seismogenic zone, *Geochem. Geophys.*
923 *Geosyst.*, 11, Q01X09, doi:10.1029/2009gc002674
- 924 Ichiyama, Y.; Tsujimori, T.; Fryer, P.; Michibayashi, K.; Tamura, A. & Morishita, T., 2021,
925 Temporal and spatial mineralogical changes in clasts from Mariana serpentinite mud volcanoes:
926 cooling of the hot forearc-mantle at subduction initiation, *Lithos*, 384–385, 105941,
927 doi:10.1016/j.lithos.2020.105941
- 928 Jackson, M. G. & Dasgupta, R., 2008, Compositions of HIMU, EM1, and EM2 from global
929 trends between radiogenic isotopes and major elements in ocean island basalts, *Earth Planet. Sci.*
930 *Lett.*, 276, 175–186, doi:10.1016/j.epsl.2008.09.23
- 931 Janney, P. E. & Castillo, P. R., 1999, Isotope geochemistry of the Darwin Rise seamounts and the
932 nature of long-term mantle dynamics beneath the south central Pacific, *J. Geophys. Res.*, 104,
933 10,571–10,589, doi:10.1029/1998jb900061
- 934 Jayko, A. S.; Blake, M. C. & Brothers, R. N., 1986, Blueschist metamorphism of the Eastern
935 Franciscan belt, northern California, *Geol. Soc. Am. Mem.*, 164, 107–123, doi:10.1130/mem164-
936 p107
- 937 Johnson, J. A.; Hickey-Vargas, R.; Fryer, P.; Salters, V. & Reagan, M. K., 2014, Geochemical
938 and isotopic study of a plutonic suite and related early volcanic sequences in the southern
939 Mariana forearc, *Geochem. Geophys. Geosyst.*, 15, 589–604, doi:10.1002/2013gc005053
- 940 Kahl, W.-A.; Jöns, N.; Bach, W.; Klein, F. & Alt, J. C., 2015, Ultramafic clasts from the South
941 Chamorro serpentinite mud volcano reveal a polyphase serpentinization history of the Mariana
942 forearc mantle, *Lithos*, 227, 1–20, doi:10.1016/j.lithos.2015.03.015
- 943 Kastner, M.; Solomon, E. A.; Harris, R. N. & Torres, M. E., 2014, Fluid origins, thermal regimes,
944 and fluid and solute fluxes in the forearc of subduction zones, in: Stein, R.; Blackman, D. K.;
945 Inagaki, F. & Larsen, H.-C. (eds.), *Earth and life processes discovered from seafloor*
946 *environments: a decade of science achieved by the Integrated Ocean Drilling Program (IODP)*,
947 Elsevier, 7, 671–733, doi:10.1016/b978-0-444-62617-2.00022-0

- 948 Kelley, K. A.; Plank, T.; Ludden, J. & Staudigel, H., 2003, Composition of altered oceanic crust
949 at ODP Sites 801 and 1149, *Geochem. Geophys. Geosyst.*, 4, 8910, doi:10.1029/2002gc000435
- 950 King, R.; Bebout, G.; Moriguti, R. & Nakamura, E., 2006, Elemental mixing systematics and Sr–
951 Nd isotope geochemistry of mélange formation: obstacles to identification of fluid sources to arc
952 volcanics, *Earth Planet. Sci. Lett.*, 246, 288–304, doi:10.1016/j.epsl.2006.03.053
- 953 Koppers, A. A. P.; Staudigel, H.; Wijbrans, J. R. & Pringle, M. S., 1998, The Magellan Seamount
954 Trail: implications for Cretaceous hotspot volcanism and absolute Pacific Plate motion, *Earth
955 Planet. Sci. Lett.*, 163, 53–68, doi:10.1016/s0012-821x(98)00175-7
- 956 Leat, P. T. & Larter, R. D., 2003, Intra-oceanic subduction systems: introduction, *Geol. Soc.
957 Spec. Pub.*, 219, 1–17, doi:10.1144/gsl.sp.2003.219.01.01
- 958 Liu, Y.; Zhang, G.; Zhang, J. & Wang, S., 2020, Geochemical constraints on CO₂-rich mantle
959 source for the Kocebu Seamount, Magellan Seamount chain in the western Pacific, *J. Oceanol.
960 Limnol.*, 38, 1201–1214, doi:10.1007/s00343-020-0013-x
- 961 Lockwood, J. P., 1972, Possible mechanisms for the emplacement of alpine-type serpentinite,
962 *Geol. Soc. Am. Mem.*, 132, 273–288, doi:10.1130/mem132-p273
- 963 Maekawa, H.; Masaya, S.; Ishill, T.; Fryer, P. & Pearce, J. A., 1993, Blueschist metamorphism in
964 an active subduction zone, *Nature*, 364, 520–523, doi:10.1038/364520a0
- 965 Manning, C. E., 2004, The chemistry of subduction-zone fluids, *Earth Planet. Sci. Lett.*, 223, 1–
966 16, doi:10.1016/j.epsl.2004.04.030
- 967 Marschall, H. R. & Schumacher, J. C., 2012, Arc magmas sourced from mélange diapirs in
968 subduction zones, *Nat. Geosci.*, 5, 862–867, doi:10.1038/ngeo1634
- 969 Menzies, C.; Price, R. E.; Ryan, J.; Sissman, O.; Takai, K.; Wheat, C. G., 2021, Spatial variation
970 of subduction zone fluids during progressive subduction: insights from serpentinite mud
971 volcanoes, *Geochim. Cosmochim. Acta*, in press, doi:10.1016/j.gca.2021.10.030
- 972 Moore, J. C. & Vrolijk, P., 1992, Fluids in accretionary prisms, *Rev. Geophys.*, 30, 113–135,
973 doi:10.1029/92rg00201
- 974 Mottl, M. J.; Wheat, C. G.; Fryer, P. B.; Gharib, J. & Martin, J. B., 2004, Chemistry of springs
975 across the Mariana forearc shows progressive devolatilization of the subducting plate, *Geochim.
976 Cosmochim. Acta*, 68, 4915–4933, doi:10.1016/j.gca.2004.05.037

- 977 Oakley, A. J., 2008, A multi-channel seismic and bathymetric investigation of the central Mariana
978 convergent margin, *PhD Thesis*, University of Hawai'i, Manoa, HI
- 979 Oakley, A. J.; Taylor, B. & Moore, G. F., 2008, Pacific Plate subduction beneath the central
980 Mariana and Izu-Bonin fore arcs: new insights from an old margin, *Geochem. Geophys. Geosyst.*,
981 9, Q06003, doi:10.1029/2007gc001820
- 982 Pabst, S.; Zack, T.; Savov, I. P.; Ludwig, T.; Rost, D.; Tonarini, S. & Vicenzi, E. P., 2012, The
983 fate of subducted oceanic slabs in the shallow mantle: insights from boron isotopes and light
984 element composition of metasomatized blueschists from the Mariana forearc, *Lithos*, 132–133,
985 162–179, doi:10.1016/j.lithos.2011.11.010
- 986 Pattison, D. R. M.; De Capitani, C. & Gaidies, F., 2011, Petrological consequences of variations
987 in metamorphic reaction affinity, *J. Metamorph. Geol.*, 29, 953–977, doi:10.1111/j.1525-
988 1314.2011.00950.x
- 989 Peacock, S. A., 1990, Fluid processes in subduction zones, *Science*, 248, 329–337,
990 doi:10.1126/science.248.4953.329
- 991 Peacock, S. A. & Wang, K., 1999, Seismic consequences of warm versus cool subduction
992 metamorphism: examples from Southwest and Northeast Japan, *Science*, 286, 937–939,
993 doi:10.1126/science.286.5441.937
- 994 Perfit, M. R.; Gust, D. A.; Bence, A. E.; Arculus, R. J. & Taylor, S. R., 1980, Chemical
995 characteristics of island-arc basalts: implications for mantle sources, *Chem. Geol.*, 30, 227–256,
996 doi:10.1016/0009-2541(80)90107-2
- 997 Plank, T. & Langmuir, C. H., 1998, The chemical composition of subducting sediment and its
998 consequences for the crust and mantle, *Chem. Geol.*, 145, 325–394, doi:10.1016/s0009-
999 2541(97)00150-2
- 1000 Plank, T.; Ludden, J. N.; Escutia, C. & et al., 2000, *Proc. ODP 185, Ocean Drilling Program, TX*,
1001 doi:10.2973/odp.proc.ir.185.2000
- 1002 Poli, S. & Schmidt, M. W., 1995, H₂O transport and release in subduction zones: experimental
1003 constraints on basaltic and andesitic systems, *J. Geophys. Res. Solid Earth*, 100, 22299–22314,
1004 doi:10.1029/95jb01570

- 1005 Pons, M.-L.; Quitté, G.; Fujii, T.; Rosing, M. T.; Reynard, B.; Moynier, F.; Douchet, C. &
1006 Albarède, F., 2011, Early Archean serpentine mud volcanoes at Isua, Greenland, as a niche for
1007 early life, *Proc. Natl. Aca. Sci.*, 108, 17639–17643, doi:10.1073/pnas.1108061108
- 1008 Putnis, A. & Austrheim, H., 2010, Fluid-induced processes: metasomatism and metamorphism,
1009 *Geofluids*, 10, 254–269, doi:10.1111/j.1468-8123.2010.00285.x
- 1010 Putnis, A. & John, T., 2010, Replacement processes in the Earth's crust, *Elements*, 6, 159–164,
1011 doi:10.2113/gselements.6.3.159
- 1012 Ringwood, A. E., 1969, Composition and evolution of the upper mantle, *Geoph. Monog. Series*,
1013 13, 1–17, doi:10.1029/gm013p0001
- 1014 Rustioni, G.; Audetat, A. & Keppler, H., 2021, The composition of subduction zone fluids and the
1015 origin of the trace element enrichments in arc magmas, *Contrib. Mineral. Petrol.*, 176, 51,
1016 doi:10.1007/s00410-021-01810-8
- 1017 Savov, I. P.; Guggino, S.; Ryan, J. G.; Fryer, P. B. & Mottl, M. J., 2005a, Geochemistry of
1018 serpentinite muds and metamorphic rocks from the Mariana forearc, ODP Sites 1200 and 778–
1019 779, South Chamorro and Conical Seamounts, in: Shinohara, M.; Salisbury, M. H. & Richter, C.
1020 (Eds.), *Proc. ODP 195, Sci. Results*, 195, 1–49, doi:10.2973/odp.proc.sr.195.103.2005
- 1021 Savov, I. P.; Ryan, J. G.; Antonio, M. D.; Kelley, K. & Mattie, P., 2005b, Geochemistry of
1022 serpentinitized peridotites from the Mariana forearc Conical Seamount, ODP Leg 125: implications
1023 for the elemental recycling at subduction zones, *Geochem. Geophys. Geosyst.*, 6, Q04J15,
1024 doi:10.1029/2004gc000777
- 1025 Savov, I. P.; Ryan, J. G.; Antonio, M. D. & Fryer, P., 2007, Shallow slab fluid release across and
1026 along the Mariana arc-basin system: insights from geochemistry of serpentinitized peridotites from
1027 the Mariana fore arc, *J. Geophys. Res.*, 112, B09205, doi:10.1029/2006jb004749
- 1028 Scambelluri, M. & Philippot, P., 2001, Deep fluids in subduction zones, *Lithos*, 55, 213–227,
1029 doi:10.1016/s0024-4937(00)00046-3
- 1030 Schmidt, M. W., 1996, Experimental constraints on recycling of potassium from subducted
1031 oceanic crust, *Science*, 272, 1927–1930, doi:10.1126/science.272.5270.1927
- 1032 Shervais, J. W., 1982, Ti-V plots and the petrogenesis of modern and ophiolitic lavas, *Earth*
1033 *Planet. Sci. Lett.*, 59, 101–118, doi:10.1016/0012-821x(82)90120-0

- 1034 Shervais, J. W., 2021, The petrogenesis of modern and ophiolitic lavas reconsidered: Ti–V and
1035 Nb–Th, *Geosci. Front.*, in press, doi: 10.1016/j.gsf.2021.101319
- 1036 Shervais, J. W.; Choi, S. H.; Sharp, W. D.; Ross, J.; Zoglman-Schuman, M. & Mukasa, S. B.,
1037 2011, Serpentinite matrix mélange: implications of mixed provenance for mélange formation,
1038 *Geol. Soc. Am. Spec. Pap.*, 480, 1–38, doi:10.1130/2011.2480(01)
- 1039 Shervais, J. W.; Reagan, M.; Haugen, E.; Almeev, R. R.; Pearce, J. A.; Prytulak, J.; Ryan, J. G.;
1040 Whattam, S. A.; Godard, M.; Chapman, T.; Li, H.; Kurz, W.; Nelson, W. R.; Heaton, D.;
1041 Kirchenbaur, M.; Shimizu, K.; Sakuyama, T.; Li, Y. & Vetter, S. K., 2019, Magmatic response to
1042 subduction initiation: part 1. Fore-arc basalts of the Izu-Bonin Arc from IODP Expedition 352,
1043 *Geochem. Geophys. Geosyst.*, 20, 314–338, doi:10.1029/2018gc007731
- 1044 Sievers, N. E.; Tenore, J.; Penniston-Dorland, S. C. & Bebout, G. E., 2016, Fingerprints of
1045 forearc element mobility in blueschist-facies metaconglomerates, Catalina Schist, California, *Int.*
1046 *Geol. Rev.*, 59, 741–752, doi:10.1080/00206814.2016.1253038
- 1047 Spandler, C. & Pirard, C., 2013, Element recycling from subducting slabs to arc crust: a review,
1048 *Lithos*, 170, 208–223, doi:10.1016/j.lithos.2013.02.016
- 1049 Staudigel, H., 2014, Chemical fluxes from hydrothermal alteration of the oceanic crust, *Treatise*
1050 *on geochemistry*, Elsevier, 583–606, doi:10.1016/b978-0-08-095975-7.00318-1
- 1051 Staudigel, H.; Plank, T.; White, B. & Schmincke, H.-U., 1996, Geochemical fluxes during
1052 seafloor alteration of the basaltic upper oceanic crust: DSDP Sites 417 and 418, *Geoph. Monog.*
1053 *Ser.*, 96, 19–38, doi:10.1029/gm096p0019
- 1054 Staudigel, H.; Koppers, A. A. P.; Plank, T. A. & Hanan, B. B., 2010, Seamounts in the subduction
1055 factory, *Oceanography*, 23, 176–181, doi:10.5670/oceanog.2010.69
- 1056 Stern, R. J., 2002, Subduction zones, *Rev. Geophys.*, 40, 4, 1012, doi:10.1029/2001rg000108
- 1057 Sudo, A. & Tatsumi, Y., 1990, Phlogopite and K-amphibole in the upper mantle: implications for
1058 magma genesis in subduction zones, *Geophys. Res. Lett.*, 17, 29–32,
1059 doi:10.1029/gl017i001p00029
- 1060 Sun, S.-s. & McDonough, W. F., 1989, Chemical and isotopic systematics of oceanic basalts:
1061 implications for mantle composition and processes, *Geological Society Special Publications*, 42,
1062 313–345, doi:10.1144/gsl.sp.1989.042.01.19

- 1063 Tamblyn, R.; Zack, T.; Schmitt, A. K.; Hand, M.; Kelsey, D.; Morrissey, L.; Pabst, S. & Savov, I.
1064 P., 2019, Blueschist from the Mariana forearc records long-lived residence of material in the
1065 subduction channel, *Earth Planet. Sci. Lett.*, 519, 171–181, doi:10.1016/j.epsl.2019.05.013
- 1066 Tamura, Y.; Tani, K.; Chang, Q.; Shukuno, H.; Kawabata, H.; Ishizuka, O. & Fiske, R. S., 2007,
1067 Wet and dry basalt magma evolution at Torishima Volcano, Izu–Bonin Arc, Japan: the possible
1068 role of phengite in the downgoing slab, *J. Petrol.*, 48, 1999–2031, doi:10.1093/petrology/egm048
- 1069 Tamura, Y.; Ishizuka, O.; Stern, R. J.; Nichols, A. R. L.; Kawabata, H.; Hirahara, Y.; Chang, Q.;
1070 Miyazaki, T.; Kimura, J.-I.; Embley, R. W. & Tatsumi, Y., 2014, Mission immiscible: distinct
1071 subduction components generate two primary magmas at Pagan Volcano, Mariana Arc, *J. Pet.*,
1072 55, 63–101, doi:10.1093/petrology/egt061
- 1073 Tang, L.; Dong, Y.; Chu, F.; Chen, L.; Ma, W. & Liu, Y., 2019, Geochemistry and age of
1074 seamounts in the West Pacific: mantle processes and petrogenetic implications, *Acta Oceanol.*
1075 *Sin.*, 38, 71–77, doi:10.1007/s13131-019-1371-0
- 1076 Tatsumi, Y. & Eggins, S., 1995, Subduction zone magmatism, *Blackwell Science*, Cambridge
- 1077 Taylor, S. R. & McLennan, S. M., 1995, The geochemical evolution of the continental crust, *Rev.*
1078 *Geophys.*, 33, 241–265, doi:10.1029/95rg00262
- 1079 Ukar, E. & Cloos, M., 2014, Low-temperature blueschist-facies mafic blocks in the Franciscan
1080 mélange, San Simeon, California: field relations, petrology, and counterclockwise *P-T* paths,
1081 *Geol. Soc. Am. Bull.*, 126, 831–856, doi:10.1130/b30876.1
- 1082 Ulmer, P., 2001, Partial melting in the mantle wedge—the role of H₂O in the genesis of mantle-
1083 derived 'arc-related' magmas, *Phys. Earth Planet. Inter.*, 127, 215–232, doi:10.1016/s0031-
1084 9201(01)00229-1
- 1085 Vannucchi, P.; Sage, F.; Phipps Morgan, J.; Remitti, F. & Collot, J.-Y., 2012, Toward a dynamic
1086 concept of the subduction channel at erosive convergent margins with implications for interplate
1087 material transfer, *Geochem. Geophys. Geosyst.*, 13, Q02003, doi:10.1029/2011gc003846
- 1088 Wakabayashi, J., 2012, Subducted sedimentary serpentinite mélanges: record of multiple burial–
1089 exhumation cycles and subduction erosion, *Tectonophysics*, 568–569, 230–247,
1090 doi:10.1016/j.tecto.2011.11.006

- 1091 Wang, K. & Bilek, S. L., 2014, Initiated review paper: Fault creep caused by subduction of rough
1092 seafloor relief, *Tectonophysics*, 610, 1–24, doi:10.1016/j.tecto.2013.11.024
- 1093 Wang, Y.; Foley, S. F. & Prelević, D., 2017, Potassium-rich magmatism from a phlogopite-free
1094 source, *Geology*, 45, 467–470, doi:10.1130/g38691.1
- 1095 Watts, A. B.; Koppers, A. A. P. & Robinson, D. P., 2010, Seamount subduction and earthquakes,
1096 *Oceanography*, 23, 166–173, doi: 10.5670/oceanog.2010.68
- 1097 Wei, W.; Kastner, M.; Deyhle, A. & Spivack, A. J., 2006, Geochemical cycling of fluorine,
1098 chlorine, bromine, and boron and implications for fluid-rock reactions in Mariana forearc, South
1099 Chamorro Seamount, ODP Leg 195, in: Shinohara, M.; Salisbury, M. H.; Richter, C. (Eds.), *Proc.*
1100 *ODP, Sci. Results*, 195, 1–23, doi:10.2973/odp.proc.sr.195.106.2005
- 1101 Wessel, P.; Smith, W. H. F.; Scharroo, R.; Luis, J. & Wobbe, F., 2013, Generic Mapping Tools:
1102 improved version released, *Eos*, 94, 409–410, doi:10.1002/2013eo450001
- 1103 Wheat, C. G.; Fournier, T.; Paul, C.; Menzies, C.; Price, R. E.; Ryan, J. & Sissman, O., 2018,
1104 Data report: IODP Expedition 366 pore water trace elements (V, Mo, Rb, Cs, U, Ba, and Li)
1105 compositions, in: Fryer, P.; Wheat, C. G.; Williams, T. & the Expedition 366 Scientists, *Proc.*
1106 *IODP*, 366, doi:10.14379/iodp.proc.366.201.2018
- 1107 White, R.W.; Powell, R. & Holland, T. J. B., 2007, Progress relating to calculation of partial
1108 melting equilibria for metapelites, *J. Metamorph. Geol.*, 25, 511–527, doi:10.1111/j.1525-
1109 1314.2007.00711.x
- 1110 White, R.W.; Powell, R. & Johnson, T. E., 2014a, The effect of Mn on mineral stability in
1111 metapelites revisited: new $a-x$ relations for manganese-bearing minerals, *J. Metamorph. Geol.*,
1112 32, 809–828, doi:10.1111/jmg.12095
- 1113 White, R.W.; Powell, R.; Holland, T. J. B.; Johnson, T. E. & Green, E. C. R., 2014b, New
1114 mineral activity–composition relations for thermodynamic calculations in metapelitic systems, *J.*
1115 *Metamorph. Geol.*, 32, 261–286, doi:10.1111/jmg.12071
- 1116 Zack, T.; Rivers, T. & Foley, S. F., 2001, Cs–Rb–Ba systematics in phengite and amphibole: an
1117 assessment of fluid mobility at 2.0 GPa in eclogites from Trescolmen, Central Alps, *Contrib.*
1118 *Mineral. Petrol.*, 140, 651–669, doi:10.1007/s004100000206

1119 Zhou, Z. & Lin, J., 2018, Elasto-plastic deformation and plate weakening due to normal faulting
 1120 in the subducting plate along the Mariana Trench, *Tectonophysics*, 734–735, 59–68,
 1121 doi.org/10.1016/j.tecto.2018.04.008

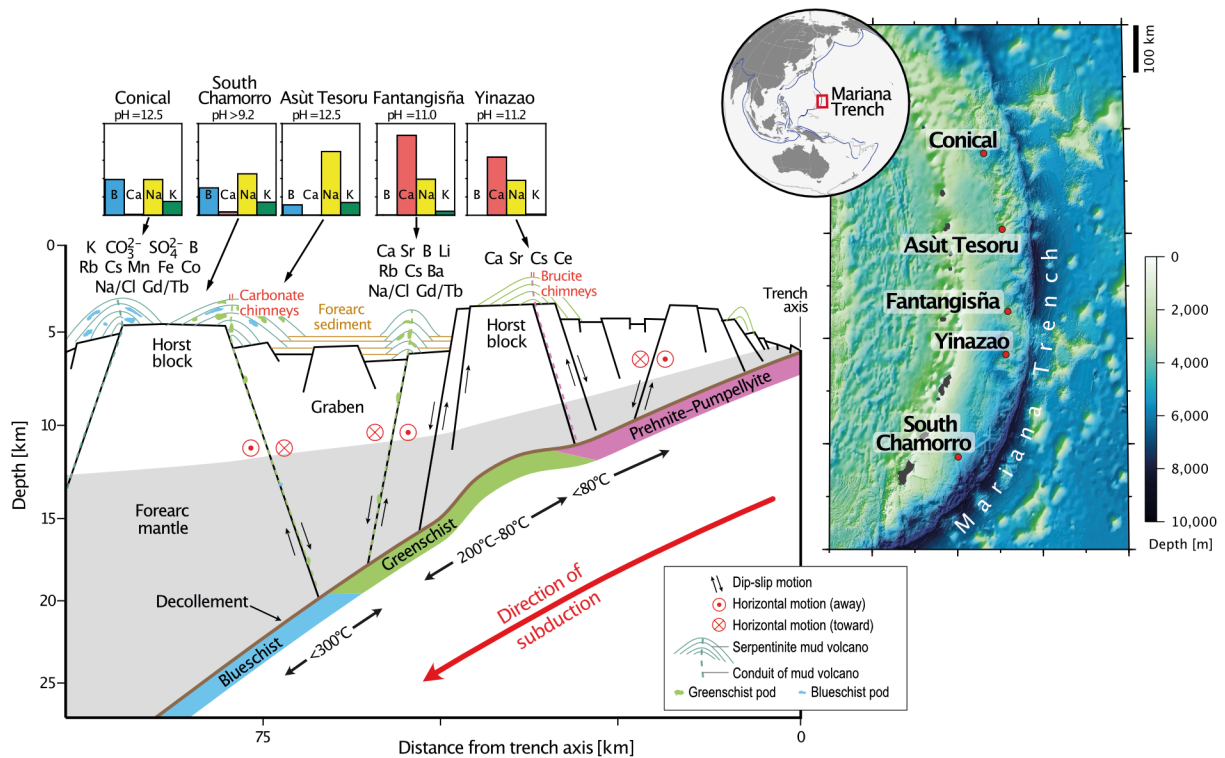
1122

1123 **11 Data Availability Statement**

1124 The original contributions presented in the study are included in the article/Supplementary
 1125 Material; further inquiries can be directed to the corresponding author.

1126

1127 **Figures**

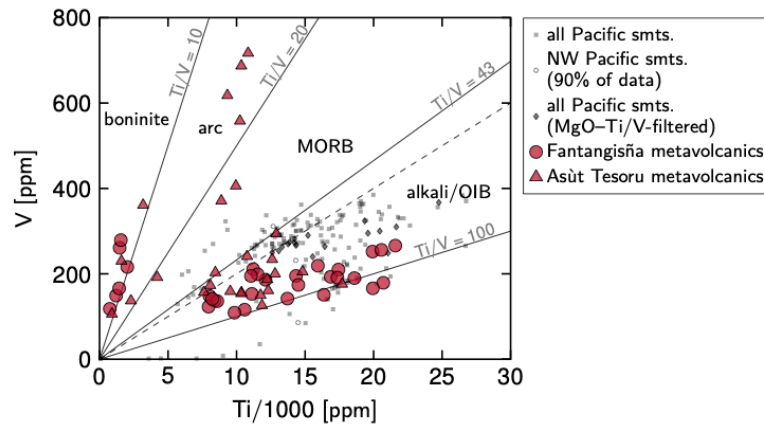


1128

1129 Figure 1: Idealized cross section of the Mariana forearc setting, from east to west, including the
 1130 relative positioning of the serpentinite mud volcanoes. Compositions of the slab-derived
 1131 serpentinite mud pore waters systematically vary across the forearc, reflecting prograde
 1132 metamorphic processes in the subducting slab. The map shows the distribution of the serpentinite
 1133 mud volcanoes drilled by ODP and IODP on the Mariana forearc. Also note the large number of
 1134 Pacific seamounts that will eventually be subducted. Modified from Fryer et al. (2018) and Wheat
 1135 et al. (2018). Globe inset and map created with Generic Mapping Tools (Wessel et al., 2013) with

1136 the Mariana Trench 6 arc-second Bathymetric Digital Elevation Model from the NOAA's
1137 National Geophysical Data Center.

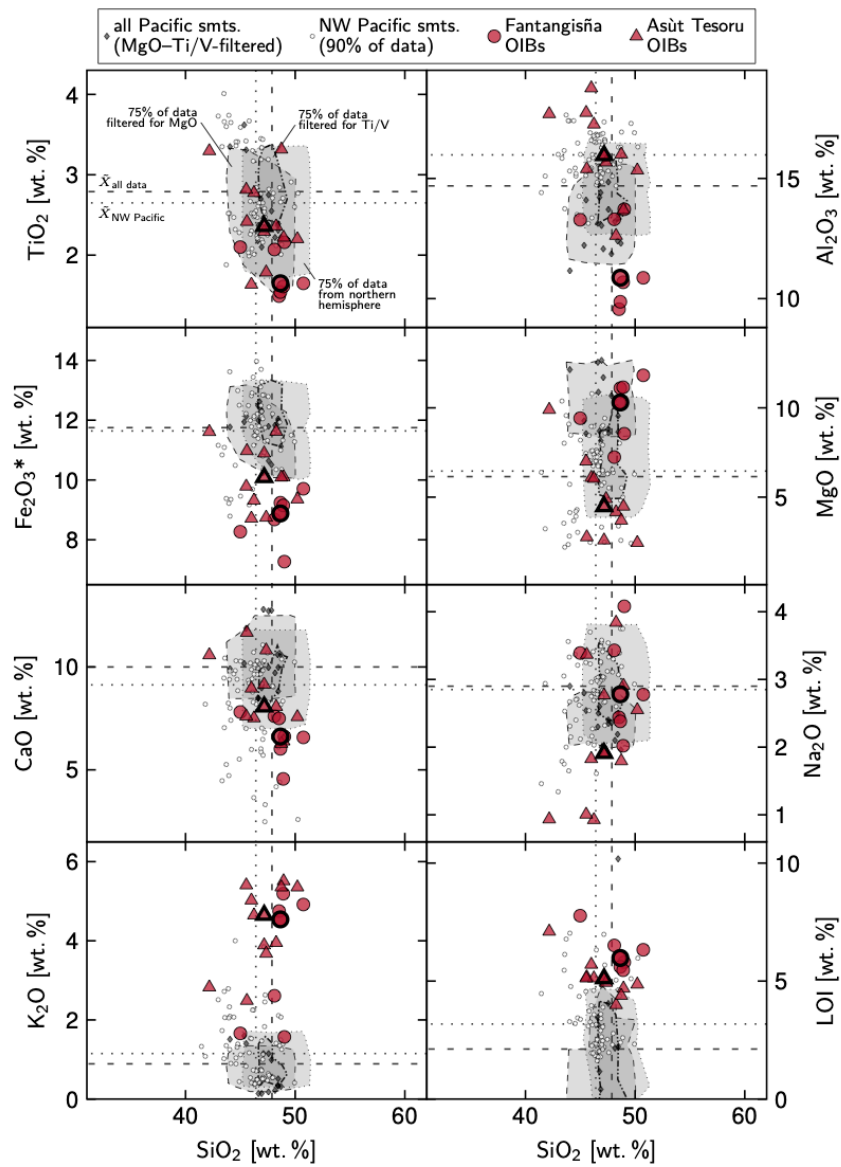
1138



1139

1140 Figure 2: Bulk rock Ti–V systematics of metamafic clasts recovered during IODP Exp. 366. An
1141 OIB provenance is implied by Ti/V ratios between 43 and 100 (Shervais, 2021; the dashed line
1142 marks the now revised discrimination line of Ti/V = 50 after Shervais, 1982) for the clasts from
1143 Fantangisña and Asùt Tesoru Seamounts that are discussed in this paper. Data from Fryer et al.
1144 (2020) and Deng et al. (2021). Compositions of Pacific seamounts are shown for comparison (see
1145 Section 2.1 for more information and data sources).

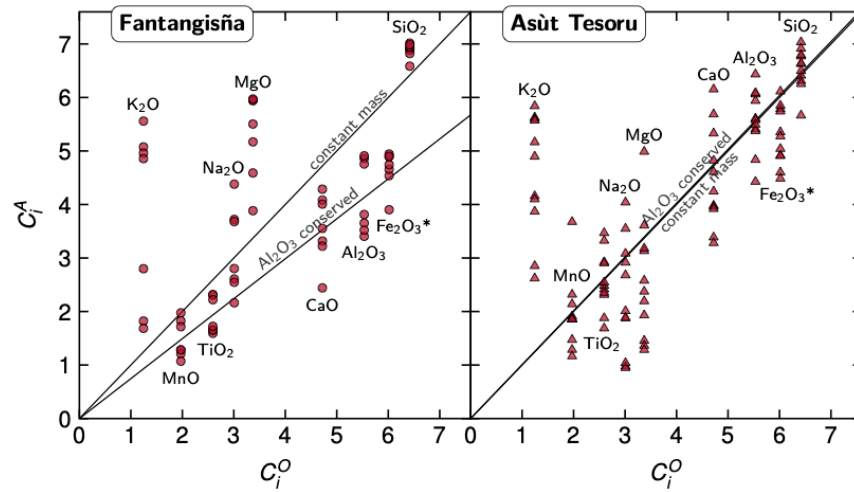
1146



1147

1148 Figure 3: Bulk compositions of recycled OIBs from Fantangisña and Asùt Tesoru Seamounts
 1149 presented in a Harker diagram. Plot marks with thick outlines illustrate median compositions of
 1150 clasts from each seamount. The clasts differ in composition (most obviously with regard to K₂O
 1151 and LOI) from Pacific Plate seamounts, implying metasomatic composition changes in the
 1152 subduction zone. Data from this study, Fryer et al. (2018), and Deng et al. (2021). Compositions
 1153 of Pacific seamounts are shown for comparison (see Section 2.1 for more information and data
 1154 sources; \tilde{x} = median compositions).

1155



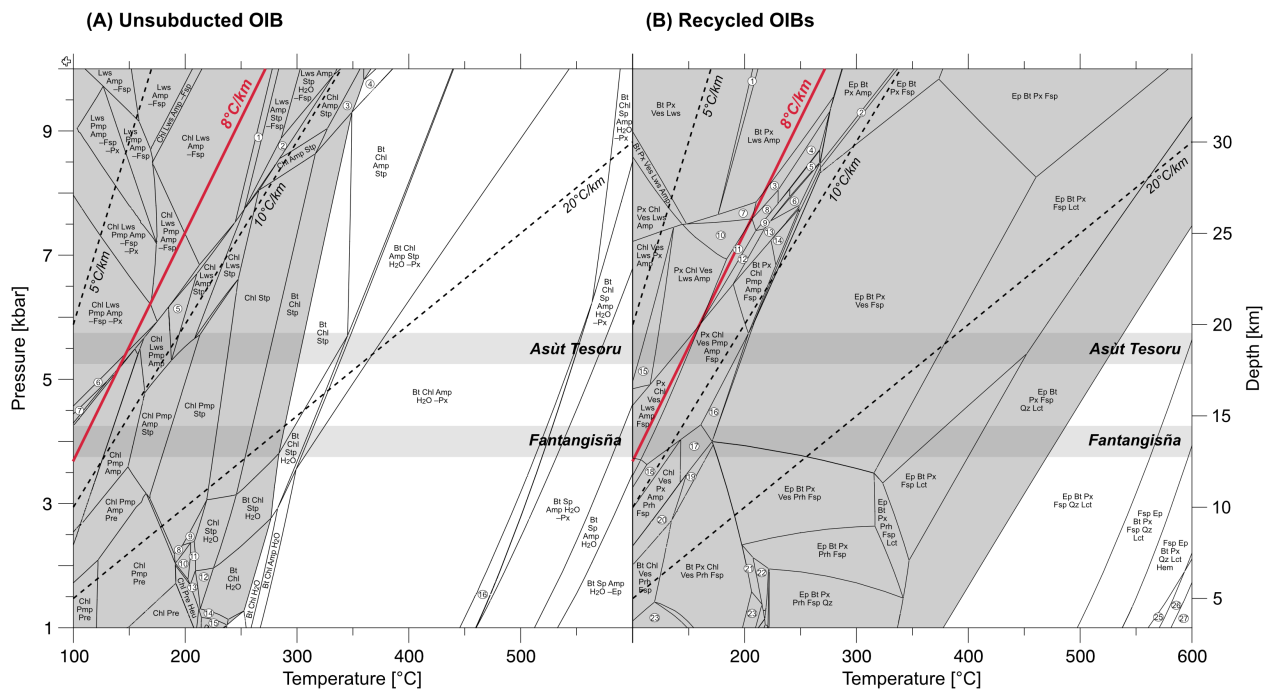
1156

1157 Figure 4: Isocon plots comparing the anhydrous compositions of the recycled OIBs (C_i^A) to the
1158 median of the NW Pacific seamounts (C_i^O). The net mass of samples from Fantangisña Seamount
1159 appears to have increased together with gains in K_2O , SiO_2 , MgO , and Na_2O , whereas the net
1160 mass of the Asùt Tesoru Seamount samples did not significantly change and the clasts are merely
1161 enriched in K_2O and some in SiO_2 . The lines shown for Al_2O_3 -conservation are based on the
1162 mean Al_2O_3 contents; at Asùt Tesoru, the lines of constant mass and Al_2O_3 -conservation are
1163 almost identical. Oxide concentrations are scaled by the following divisors: SiO_2 , 7.5; Al_2O_3 , 3;
1164 $Fe_2O_3^*$, 2; MnO , 0.1; MgO , 2; CaO , 2.

1165

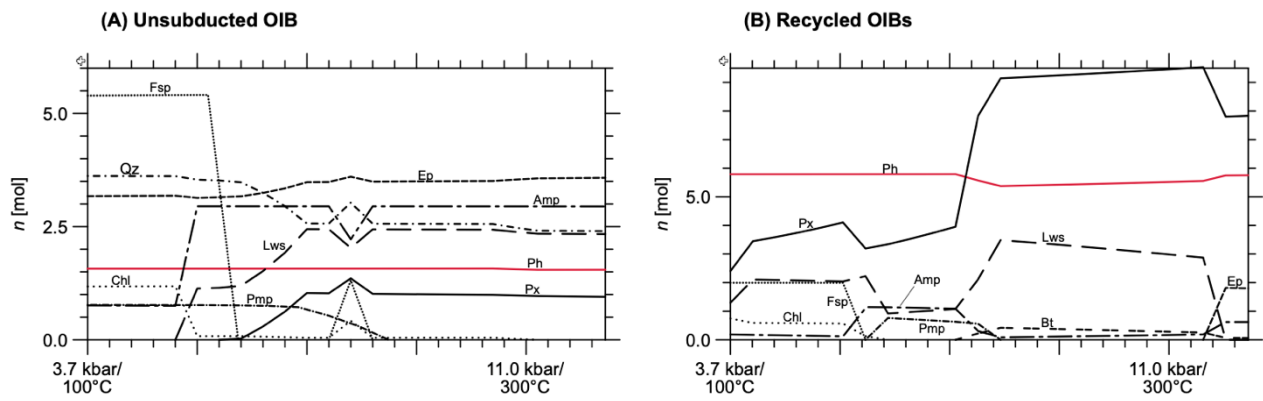
1166

1167



1168

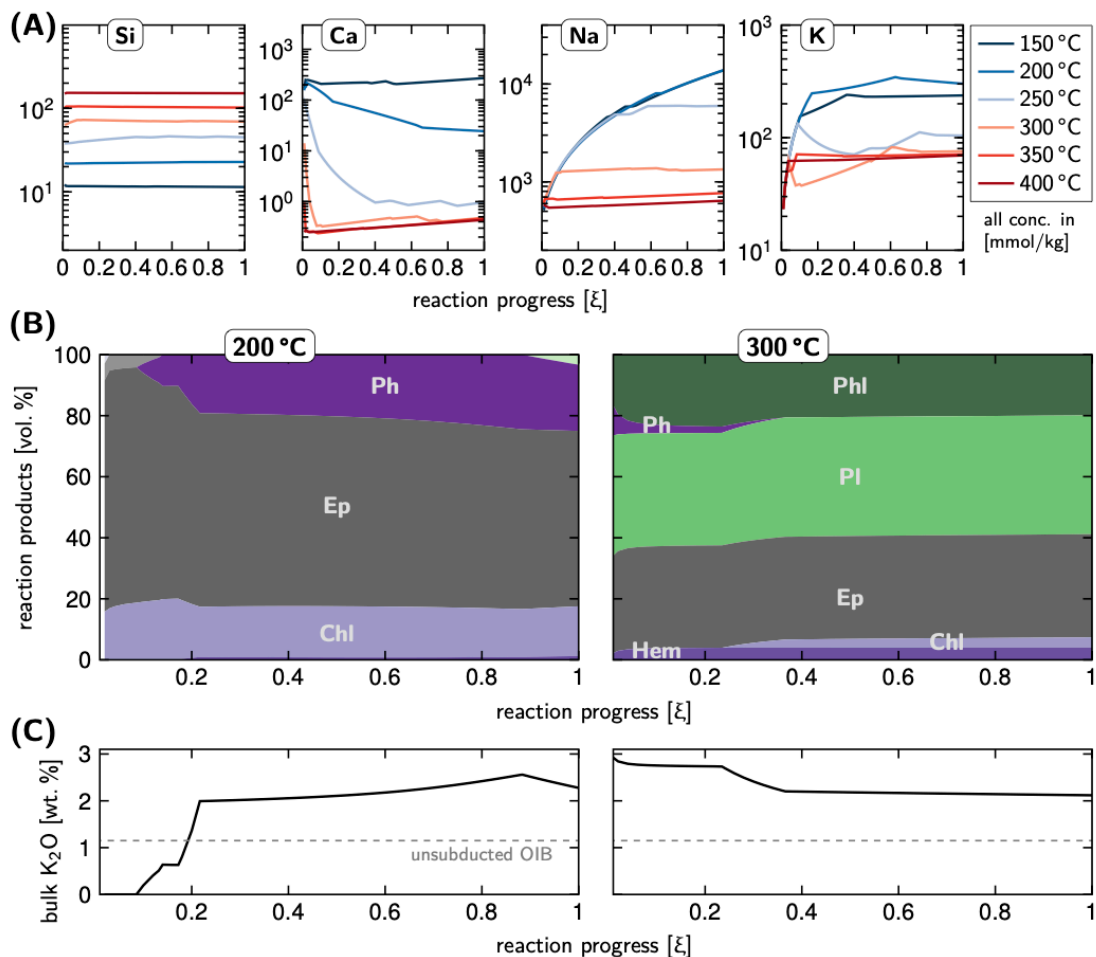
1169 Figure 5: Equilibrium assemblage diagrams for (A) unsubducted OIB and (B) OIBs recycled by
 1170 the serpentinite mud volcanoes. The predicted stability of phengite is indicated by the gray
 1171 background. Note the considerably larger stability field of phengite in the metasomatized,
 1172 recycled OIBs . Quantities of metamorphic phases along the 8°C/km geotherms (red lines) are
 1173 shown in Fig. 6. Estimated P conditions at the top of the slab beneath Fantangisña and Asút
 1174 Tesoru Seamounts are indicated by gray bars. In (A): Qz, Fsp, Ep, and Px are present at all P/T
 1175 conditions, unless indicated otherwise; 1, Chl Lws Amp Stp –Fsp; 2, Lws Amp Stp; 3, Bt Chl
 1176 Amp Stp; 4, Bt Chl Amp Stp; 5, Chl Lws Amp; 6, Chl Lws Pmp Amp –Px; 7, Chl Pmp Amp –Px;
 1177 8, Chl Pmp Stp Heu; 9, Chl Pmp Stp H₂O; 10, Chl Stp Heu; 11, Chl Stp Heu H₂O; 12, Chl H₂O;
 1178 13, Chl Heu H₂O; 14, Bt Chl Heu H₂O; 15, Bt Chl Heu; 16, Bt Chl Amp H₂O –Px. In (B): H₂O is
 1179 present at all P/T conditions, unless indicated otherwise; 1, Bt Px Lws; 2, Ep Bt Px Amp Fsp; 3,
 1180 Bt Px Lws Pmp Amp; 4, Px Lws Pmp Amp; 5, Px Pmp Amp Fsp; 6, Bt Px Pmp Amp Fsp; 7, Bt
 1181 Px Ves Lws Amp; 8, Px Lws Pmp Amp; 9, Px Pmp Amp Fsp; 10, Bt Px Ves Lws Amp; 11, Px
 1182 Ves Lws Pmp Amp; 12, Px Ves Pmp Amp Fsp; 13, Bt Px Pmp Amp Fsp; 14, Bt Px Chl Pmp Fsp;
 1183 15, Chl Ves Lws Px Amp; 16, Ep Px Chl Ves Amp Fsp; 17, Px Chl Ves Amp Prh Fsp; 18, Chl
 1184 Ves Pmp Px Amp Prh Fsp; 19, Bt Px Chl Ves Amp Prh Fsp; 20, Bt Chl Ves Amp Prh Fsp; 21, Ep
 1185 Bt Px Chl Prh Fsp; 22, Ep Bt Px Prh Stp Fsp; 23, Bt Chl Ves Prh Fsp Stp; 24, Bt Px Chl Prh Fsp;
 1186 25, Fsp Bt Px Qz Lct Hem; 26, Fsp Bt Px Sp Qz Lct Hem; 27, Fsp Bt Px Sp Qz Lct.
 1187 Abbreviations: Amp, amphibole; Bt, biotite; Chl, chlorite; Ep, epidote; Fsp, feldspar; Hem,
 1188 hematite; Heu, heulandite; Lct, leucite; Lws, lawsonite; Pmp, pumpellyite; Prh, prehnite; Px,
 1189 pyroxene; Qz, quartz; Sp, spinel; Stp, stilpnomelane; Ves, vesuvianite.



1190

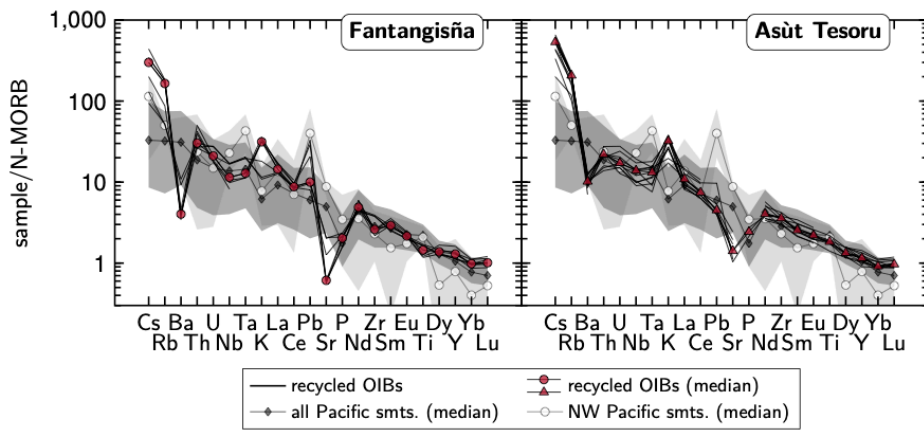
1191 Figure 6: Mineral assemblages and quantities as predicted for (A) unsubducted OIB and
 1192 (B) recycled OIBs along an 8°C/km geotherm. In addition to the much larger stability field of
 1193 phengite (see Fig. 5b) it is also remarkably higher amounts of phengite that are predicted for the
 1194 composition of the recycled OIBs. In (A), amphibole is tremolitic at low P/T and glaucophane–
 1195 riebeckite above ~5–6 kbar/150°C, pyroxene is diopside to aegirine in composition (see also
 1196 Fig. S3a). Amphibole in (B) is glaucophane to riebeckite, and pyroxene includes components of
 1197 diopside, aegirine, and jadeite (Fig. S3b); biotite is phlogopitic. Phases with abundances <0.5 mol
 1198 are not shown; these are the zeolite-group mineral stilbite (at 3.5 kbar/100°C) and vesuvianite (up
 1199 to ~7 kbar/200°C) in (B). Abbreviations: Amp, amphibole; Ph, phengite; others as in Fig. 5.

1200



1201

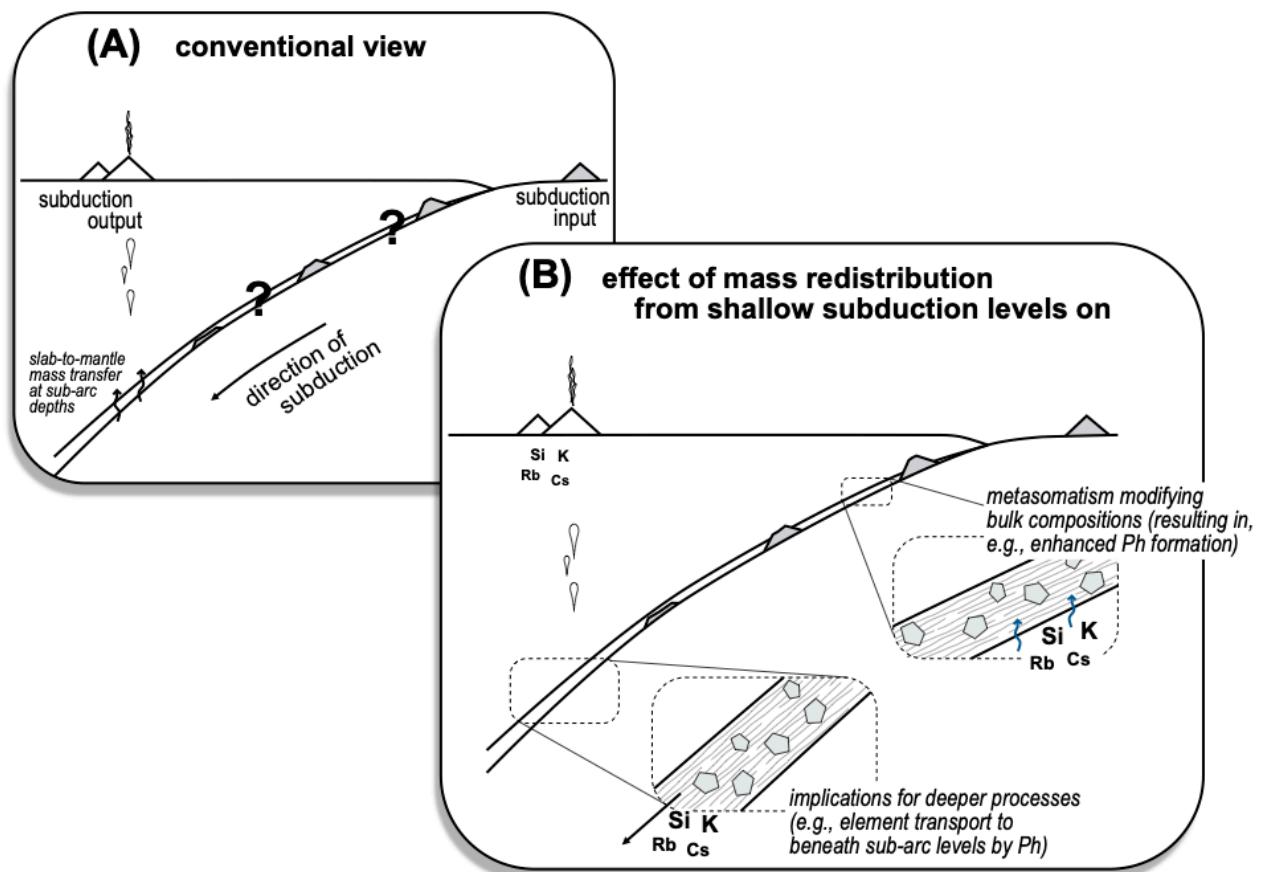
1202 Figure 7: Results of reaction path models. The x-axes depict decreasing f/r ratios (with increasing
 1203 reaction progress, ξ). (A) Modeled solute concentrations in a fluid after its equilibration with
 1204 AOC (composition from Staudigel, 2014) at $P = 5$ kbar, varying T , and a f/r ratio of 0.1 at $\xi = 1$.
 1205 Fluids equilibrated with AOC in a rock-dominated system, as is likely the case in subducting
 1206 lithosphere, contain generally high K and Na; at $T < 200^\circ\text{C}$, these solutes are particularly
 1207 enriched. Calcium contents are also high at low T ; those of Si increase with increasing T .
 1208 Corresponding phase assemblages are shown in Figure S8. (B) Equilibrium phase assemblage
 1209 predictions for OIB (median composition of NW Pacific seamounts; cf. Tab. 3) after the reaction
 1210 with AOC-derived fluids shown in (A) at 200°C and 300°C , respectively, with f/r ratios of 10 at ξ
 1211 = 1. At 200°C , phengite is predicted at variable f/r ratios; at 300°C , phengite forms at high f/r
 1212 ratios whereas the dominating K-bearing phase at lower f/r ratios is phlogopite. (C) Bulk rock
 1213 K_2O contents that correspond to the phase assemblages in (B). At both T , K_2O of the
 1214 metasomatized OIBs is markedly enriched relative to the starting composition (median NW
 1215 Pacific seamount with $\text{K}_2\text{O} = 1.15$ wt.%; dashed line). Abbreviations: Ph, phengite; Phl,
 1216 phlogopite; Pl, plagioclase; others as in Fig. 5.



1217

1218 Figure 8: Multi-element diagram for the recycled OIBs from Fantangisña and Asùt Tesoru
 1219 Seamonts normalized to N-type mid-ocean ridge basalt (Sun & McDonough, 1989). Data for the
 1220 recycled OIBs are from Fryer et al. (2018; 2020) and Deng et al. (2021). Values of K, P, and Ti
 1221 are calculated from wt% oxide. Compositions of Pacific seamonts are shown for comparison
 1222 (the dark gray and light gray fields represent the ranges in composition of all Pacific seamonts
 1223 and NW Pacific seamonts, respectively, without the upper and lower 12.5% to account for
 1224 outliers; note that <20 analyses are available for the NW Pacific seamonts except for K with $n =$
 1225 67 and Ti with $n = 62$, and that no Ba analyses are available; see Section 2.1 for more information
 1226 and data sources).

1227



1228

1229 Figure 9: Interpretative conceptual sketch of metasomatism at shallow depths and its implications.

1230 (A) Conventional approach in which subduction inputs are compared with arc volcano outputs.

1231 This concept mostly takes account of subduction metamorphism affecting incoming lithologies,

1232 but metasomatism is in many cases ignored. (B) Mass transfer and metasomatism within the

1233 subduction system occur from very shallow levels on. These processes can produce entirely new

1234 bulk compositions with mineral assemblages that differ from those in the metamorphosed

1235 subducting lithologies of (A). Such shallow subduction processes can affect element

1236 redistribution and cycling at deeper levels. In this study we demonstrate that K and other solutes

1237 are mobilized in the Mariana Subduction Zone at $T \leq 200^\circ\text{C}$; they are subsequently picked up in

1238 metavolcanics and incorporated in phengite, which likely transports them into the deep mantle.

1239

1240 **Tables**

1241 Table 1: Summarized bulk rock compositional characteristics of the recycled OIBs. Data are from this study and from Fryer et al. (2018) and
 1242 Deng et al. (2021); all data in wt%.

	SiO ₂	TiO ₂	Al ₂ O ₃	Fe ₂ O ₃ *	MnO	MgO	CaO	Na ₂ O	K ₂ O	Sum	LOI
median	48.18	2.18	14.53	9.34	0.17	6.55	7.59	2.49	4.59	99.91	5.31
min	42.17	1.49	9.56	7.27	0.1	2.45	4.56	0.93	1.57	97.94	3.99
max	50.74	3.32	18.76	11.62	0.35	11.82	11.67	4.08	5.51	100.2	7.77
σ	2.04	0.54	2.73	1.12	0.06	3.11	1.77	0.93	1.28	0.64	0.92

1243 Note: Fe₂O₃* = FeO + Fe₂O₃; LOI, loss on ignition.

1244 σ = standard deviation = $\sqrt{(\sum (x(i) - \text{mean}(x))^2) / n}$

1245

1246 Table 2: Reference bulk rock compositions of Pacific seamounts (see Section 2.2). All data in wt%, except for Ti and V (in $\mu\text{g g}^{-1}$).

		SiO ₂	TiO ₂	Al ₂ O ₃	Fe ₂ O ₃ *	MnO	MgO	CaO	Na ₂ O	K ₂ O	LOI	Ti	V	Ti/V
All data	median	47.88	2.79	14.69	11.75	0.17	6.15	10.00	2.90	0.89	2.12	16260	278	53.1
	σ	4.29	0.99	2.32	2.41	0.21	4.22	2.82	1.10	1.15	2.54	5457	95.5	434.3
	<i>n</i>	2382	2391	2382	2375	2357	2417	2380	2376	2441	731	241	1152	152
N hemisphere	median	48.30	2.62	14.10	11.90	0.17	6.47	9.98	2.66	0.64	2.02	14717	268	51.2
	σ	3.66	0.81	2.28	1.98	0.05	4.46	2.54	0.99	0.98	2.52	3936	85.0	33.6
	<i>n</i>	1291	1292	1289	1291	1291	1291	1289	1293	1326	433	143	600	128
NW Pacific	median	46.40	2.65	16.00	11.60	0.20	6.50	9.10	2.90	1.15	3.20	14320	255	72.0
	σ	3.58	0.73	1.47	2.35	0.07	2.74	2.73	0.76	1.69	1.72	2331	85.8	39.2
	<i>n</i>	91	84	86	74	86	86	86	86	86	74	7	85	7
MgO-filtered	median	47.49	2.38	13.00	11.64	0.17	9.96	10.11	2.36	0.49	1.03	12660	268	49.6
	σ	2.82	0.77	1.91	1.58	0.03	1.97	2.05	0.46	0.55	2.46	4890	47.9	10.3
	<i>n</i>	431	430	433	430	427	437	433	430	431	180	48	274	36
Ti/V-filtered	median	47.47	2.93	14.29	11.94	0.17	6.47	9.92	2.90	0.95	2.16	17831	282	61.3
	σ	2.07	0.63	1.84	1.38	0.05	3.51	2.08	0.95	0.69	3.71	3592	62.5	13.5
	<i>n</i>	75	75	75	75	75	75	75	75	75	55	75	75	75
MgO–Ti/V-filtered	median	47.10	2.39	13.20	11.94	0.17	10.00	9.97	2.40	0.42	3.14	15213	273	53.7
	σ	1.22	0.43	1.04	0.68	0.01	1.45	1.38	0.30	0.50	2.69	3576	30.8	9.6
	<i>n</i>	17	17	17	17	17	17	17	17	17	9	17	17	17

1247 Note: Fe₂O₃* = FeO + Fe₂O₃; LOI = loss on ignition.

1248 σ = standard deviation = $\sqrt{(\sum (x(i) - \text{mean}(x))^2) / n}$

1249 *n* = number of analyses

1250

1251 Table 3: Results of isocon analysis, relative to OIB from the NW Pacific (cf. Tab. 2), assuming the conservation of Al₂O₃. Calculations were
 1252 done on an anhydrous basis.

Sample	Mud volcano	Reference	SiO ₂	TiO ₂	Al ₂ O ₃	Fe ₂ O ₃ *	MnO	MgO	CaO	Na ₂ O	K ₂ O
U1497A-8F-2, 14–17 cm	Fantangisña	Deng et al. (2021)	1.17	1.01	1.00	0.86	1.14	1.75	1.03	1.41	1.67
U1497A-11G-CC, 22–25 cm	Fantangisña	Deng et al. (2021)	1.23	1.01	1.00	0.73	1.04	1.53	0.85	1.64	1.53
U1497A-12F-1, 78–81 cm	Fantangisña	Deng et al. (2021)	1.25	1.00	1.00	0.90	1.01	1.34	1.01	1.42	2.62
U1498B-23R-1, 60–63 cm	Fantangisña	Deng et al. (2021)	1.75	1.00	1.00	1.28	1.06	2.65	1.38	1.41	6.62
U1498B-23R-1, 67 cm	Fantangisña	this study	1.61	0.97	1.00	1.23	0.93	2.68	1.06	1.41	6.03
U1498B-23R-1, 67–69 cm	Fantangisña	Deng et al. (2021)	1.70	1.00	1.00	1.29	1.02	2.77	1.07	1.33	6.13
U1498B-23R-1, 70–75 cm	Fantangisña	Deng et al. (2021)	1.58	0.96	1.00	1.18	0.79	2.57	0.75	1.04	6.48
U1496B-8X-CC, 0–2 cm	Asùt Tesoru	Deng et al. (2021)	1.32	1.20	1.00	1.27	0.93	0.81	1.12	1.68	4.17
U1496B-8X-CC, 0–4 cm	Asùt Tesoru	Fryer et al. (2018)	1.02	1.00	1.00	0.98	0.96	0.44	1.33	1.21	2.15
U1496B-8X-CC, 8–13 cm	Asùt Tesoru	Fryer et al. (2018)	1.02	0.92	1.00	0.94	0.96	0.40	1.01	0.96	3.25
U1496B-8X-CC, 30–32 cm	Asùt Tesoru	Fryer et al. (2018)	1.13	0.92	1.00	0.84	0.67	0.39	0.87	0.92	4.65
U1496B-8X-CC, 33–41 cm	Asùt Tesoru	Deng et al. (2021)	1.23	1.04	1.00	1.02	0.68	0.81	0.82	1.17	5.37
U1496B-10F-2, 0–5 cm	Asùt Tesoru	Fryer et al. (2018)	1.05	1.33	1.00	0.87	1.85	0.57	0.69	0.62	4.46
U1496B-10F-2, 5–8 cm	Asùt Tesoru	Fryer et al. (2018)	1.04	0.73	1.00	0.77	1.09	0.77	1.21	0.67	3.13
U1496B-10F-2, 13 cm	Asùt Tesoru	this study	0.85	0.56	1.00	0.64	0.81	0.80	0.84	0.54	3.57
U1496B-10F-2, 14 cm	Asùt Tesoru	this study	0.89	1.02	1.00	0.76	0.85	0.97	0.75	0.31	4.07
U1496B-10F-2, 17–20 cm	Asùt Tesoru	Fryer et al. (2018)	0.92	1.03	1.00	0.74	0.87	0.86	0.77	0.30	3.59
U1496B-10F-2, 35 cm	Asùt Tesoru	this study	0.82	1.19	1.00	0.91	1.10	1.38	1.05	0.29	2.13

1253 Note: Fe₂O₃* = FeO + Fe₂O₃; LOI, loss on ignition.

1254